NPL REPORT ENG 54

Review of data fusion for surface topography measurement

J Wang, R K Leach, X Jiang

SEPTEMBER 2014

Review of data fusion for surface topography measurement

Jian Wang[1,2], Richard K Leach[1,3], Xiangqian Jiang[2]
[1]Engineering Measurement Division, NPL
[2]EPSRC Centre for Innovative Manufacturing in Advanced Metrology, University of Huddersfield
[3]Current address: Department of Mechanical, Materials and Manufacturing Engineering, University of Nottingham

ISSN 1754-2987

National Physical Laboratory
Hampton Road, Teddington, Middlesex, TW11 0LW

Approved on behalf of NPLML by Dr Andrew Lewis, Science Area Leader, Dimensional Metrology

CONTENTS

LIST OF FIGURES

LIST OF TABLES

EXECUTIVE SUMMARY

The recent development of structured surfaces, freeform surfaces, and other functional engineering surfaces, challenges instruments for the measurement of surface geometry. It is often difficult to fully characterise such surfaces with a single instrument, due to the instrumental limitations of scanning range, speed, resolution or accuracy. Measurement of such surfaces using a number of different sensors is one potential solution. Such hybrid methods acquire data from different sensors and fuse the data into a unified system to achieve greater reliability or larger measurement ranges, which any individual sensor cannot achieve. As the central computation required for a multi-sensor-based technique, data fusion methods in surface topography measurement are reviewed in this report.

A data fusion framework normally includes independent computational tasks such as registration, fusion, and pre- or post-processes, for example filtration and data compression. A combination of different algorithms for each task forms different fusion solutions, including repeated measurements fusion, stitching, range image fusion and three-dimensional data fusion (3DDF). In this report, the four fusion solutions have been reviewed, with an emphasis on 3DDF algorithms. In particular, two important 3DDF algorithms, *i.e.* the weighted least squares fusion and Gaussian process (GP) fusion, are compared in terms of fusion accuracy. The advantages of the two algorithms are summarised and future work is proposed.

1 INTRODUCTION

Data fusion, or multi-sensor data fusion [1], is an emerging field which has been applied in various disciplines, such as sensor networks, robotics, video and image processing, intelligent systems and metrology. In surface metrology, there has been little research into data fusion.

During the last two decades, the manufacture of functional surface-related products, for example solar cells, medical implants, thermal conductors, and wear resistance bearings, has seen rapid progress [2, 3]. These functional surfaces are mainly formed from structured and freeform surfaces [4]. Structured and/or freeform surfaces usually have high dynamic range (HDR) properties, *i.e.* they have machined geometrical structures on the micro- or nano-scale, and have large working areas which have sizes of tens to thousands of millimetres. The HDR properties of these surfaces are challenging the current metrological techniques regarding the synchronous requirements for higher measurement precision/accuracy, larger range and higher measurement efficiency/speed [5].

One solution to the HDR challenge is integration of multiple sensors or instruments into a unified system. Some commercial instrument manufacturers are working towards this solution. For example, the Leica DCM8 surface metrology system integrates interferometry and focus variation microscopy to increase the versatility of the system [6]. WITec GmbH [7] integrates confocal Raman microscopy, atomic force microscopy and scanning near-field optical microscopy into a system which is capable of relatively fast measurement of large-area samples. These commercial systems simply combine the sensors into a common system without integration of the data from different sensors. Data fusion is a further step in these developments, which combines the datasets from multiple sensors to achieve improved data output.

The definitions of the term "data fusion" in different applications vary [1]. In surface metrology or dimensional metrology, very limited work on data fusion has been carried out [8-11], but data fusion normally refers to [11]:

> *The process of combining data from several information sources (sensors) into a common representational format in order that the metrological evaluation can benefit from all available sensor information and data.*

A consensus in academia is that data fusion [11-14] can be expected to unite the advantages of different sensors or instruments to obtain improved information. Consider, for example [12], the measurement of the length of a gauge block with a laser interferometer. The distance measured by the interferometer depends on the refractive index of air, which in turn depends on air temperature, pressure and humidity. The length of the gauge block also depends on its own temperature, so this also has to be monitored. Thus, in order to estimate the gauge block length, at least five sensors are required to measure interferometer fringe counts, air temperature, pressure, humidity and artefact temperature.

Regarding the current applications of data fusion in surface metrology, the potential benefits include some of the following [15]:

1) increased spatial coverage or measuring range;
2) increased sample density or resolution;

3) improved reliability or fidelity, *i.e.* improved accuracy with improved robustness to sensory and algorithmic uncertainty;
4) reduced measuring duration; and
5) reduced data size.

Many mature technologies and commercial instruments for surface topography measurement have been developed, including interferometry, focus variation systems, atomic force microscopy, confocal microscopy, coordinate measuring machines, structured light projection and others [11, 16]. These instruments provide a great deal of versatility with different uncertainty, resolution, measuring range, and speed. A well-chosen combination of the measuring instruments can often overcome the shortage of a single all-purpose instrument.

Fusion of surface metrological data is computationally-intensive. It usually requires several computational tools which successively carry out tasks, such as pre-processing, registration, fusion and post-processing (see Figure 1-1). Registration and fusion are the main tasks in a complete data fusion framework. Registration is responsible for linearly transforming multiple datasets into a common coordinate system. Fusion is responsible for merging the redundant data in the overlapping areas of given datasets, so that only one set of measurement data exists at all the sample positions. Pre-processes prepare input data in a form appropriate for registration and fusion. Post-processes prepare fusion output in a manner appropriate for rendering, manipulation and storage.

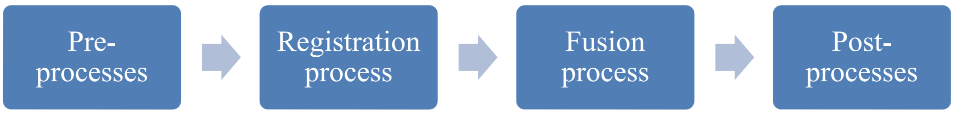

Figure 1-1. Several computational tasks in a data fusion framework.

According to the definition given above, data fusion refers to the whole process of data combination until improved information is achieved [9, 11]. In many situations, data fusion is used to refer to the fusion process between registration and post-processes within a complete data fusion framework [8]. To avoid ambiguity in this report, fusion and data fusion both refer to the complete data fusion process, including pre- and pro-processes, registration and the actual fusion process, if not specifically stated otherwise. The fusion process is used to refer to the process of real fusion work between registration and post-processes. Fusion methods or algorithms refer to the methods or algorithms used in the actual fusion process, excluding those in registration or other processes.

There are already mature fusion solutions and measurement frameworks, for example stitching interferometry [17, 18]. However, for complex input data, such as sample density-varying range images and point clouds, fusion solutions are very limited and their performance is questionable.

1.1 SOLUTION OVERVIEW

Considering the fusion of surface metrological data, the datasets to be fused can be from the same sensor under the same conditions (for example, the sampling conditions, illumination and temperature), the same sensor under different conditions, different sensors (for example, different objectives or scanning tips) or different instruments. Based on the characteristics of the datasets to be fused, data fusion in surface topography measurement can be classified into four categories: repeated measurements fusion, stitching, range image fusion and three-dimensional data fusion (3DDF). The different data fusion categories tackle different fusion situations in which the input data have different forms. Therefore, the computational complexity of each fusion category varies. In this report, the existing fusion solutions corresponding to the four fusion situations for surface metrological data are reviewed.

Repeated measurements fusion is usually undertaken for improved measurement reliability. Repeated measurements fusion tackles datasets from the same sensor at the same sampling positions. Other measuring conditions can vary, for example the illumination intensity. Hence the measurement data taken under the same or different measuring conditions can compete with or compensate each other. In this data fusion category, the sample values from different datasets on each sampling position can simply be fused in a point-wise manner. A review of this simplest data fusion technique is given in Section 2.

Stitching, which is widely used in sub-aperture stitching interferometry, is usually undertaken to expand the measuring range (for example, in a horizontal sample plane). Stitching tackles data in the forms of areal data or range images from the same sensor at different sample positions, but with the same sample conditions, *i.e.* the same sample densities and size. Each dataset for stitching must have a large enough overlapping sample region to ensure that the data can be matched to an acceptable accuracy level. The sample conditions of the data to be stitched are the same; hence a point-wise fusion can be implemented on all sample positions within the overlapping areas. Stitching is reviewed in Section 2 with interesting case studies.

Range image fusion (or cross-sensor stitching) is a generalisation of stitching. Range image fusion involves areal data or range images from the same or different sensors under different sampling conditions. Range image fusion can usually be used to obtain an improvement in measurement resolution and reliability, or an expansion of measurement range. A re-sample process is usually needed before the fusion process, so that the data can be fused in a point-wise manner. A review of range image fusion techniques is given in Section 4.

3DDF, which involves data in the form of point clouds or a mix of point clouds with range images, is reviewed in Section 5 where an introduction to the existing solutions and simulations is given.

From repeated measurements fusion, to stitching, range image fusion and 3DDF, the complexity of the input data for fusion increases. The relationships between the application scopes of the four fusion categories are shown in Figure 1-2, which implies that a fusion problem with simpler data input can be resolved using the solutions that tackle more complex data, but not *vice versa*.

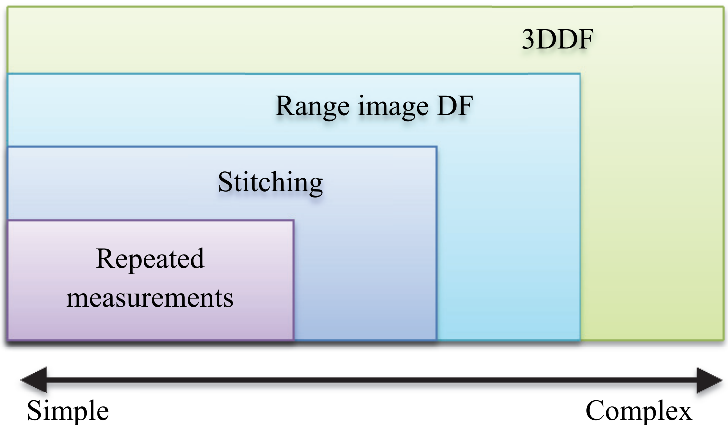

Figure 1-2. Application scopes of the four data fusion categories in surface topography measurement.

Different data fusion solutions process different forms of data. Table 1-1 presents the key differences of the computational work, *i.e.* registration and fusion processes, involved in each data fusion category. For example, repeated measurements fusion applies the simple mean for the fusion process without registration; stitching employs a three-degrees-of-freedom (DoF) registration and a simple mean for the fusion process.

In the following sections, the computational work involved in the different data fusion categories is reviewed by focusing on the fusion methods in the actual fusion processes. Research on registration can be found elsewhere [19-21].

Table 1-1. The main computational work involved in different fusion categories.

Fusion situations / solutions	Registration	Fusion process
Repeated measurements fusion	NA	Simple mean / min / max
Stitching	3-DoF registration	Simple mean
Range image fusion	3- /6-DoF registration	Weighted mean
3DDF	6-DoF registration	GP fusion / weighted mean
Others	Others	Others

2 REPEATED MEASUREMENTS FUSION

Repeated measurement is well-known in metrology to reduce measurement uncertainty. Independent measurement data from the same sensor is obtained and an arithmetic mean of the data can be calculated. If each dataset is subject to random noise (excluding systematic errors) or defects are induced by different environmental conditions, for example temperature, vibration and electromagnetic fields, the mean can have higher precision [22] (only the random uncertainty reduced).

For example, the arithmetic mean of two uncertainty-equivalent observations has a lower uncertainty than the individual observations. Assume Sensor 1 provides the measured result y_1 with a standard random uncertainty σ_1 and Sensor 2 provides the result y_2 with a standard random uncertainty σ_2, the arithmetic mean $y_F = \frac{1}{2}(y_1 + y_2)$ has the fused standard random uncertainty

$$\sigma_F = \sqrt{\sigma_1^2 + \sigma_2^2}/2\ , \tag{1}$$

which is smaller than σ_1 and σ_2 if $\sigma_1 \approx \sigma_2$.

If results $\{y_i\}$ (i = 1, 2, …, n) with similar uncertainties $(\sigma_1, \sigma_2, \dots, \sigma_n)$ are fused using the arithmetic mean, *i.e.*

$$y_F = \frac{1}{n}\sum y_i\ , \tag{2}$$

the fusion standard uncertainty is given by

$$\sigma_F = \sqrt{\sigma_1^2 + \sigma_2^2 + \cdots + \sigma_n^2}/n\ . \tag{3}$$

To have a reduced uncertainty, *i.e.* $\sigma_F < \min \sigma_i$, a sufficient but not necessary condition is that

$$\sigma_{\max} < \sqrt{\frac{(n^2-1)}{n-1}}\sigma_{\min}, \tag{4}$$

i.e. the maximum individual uncertainty is less than $\sqrt{\frac{(n^2-1)}{n-1}}$ times the minimum individual uncertainty. Otherwise, the arithmetic mean may not have a reduced uncertainty than that for each individual result.

In practical surface measurement, repeated measurements are usually implemented by keeping the environmental conditions of individual measurements the same, which means that the individual uncertainties are approximately equivalent. Therefore, the arithmetic mean fusion can usually provide a reduction of the measurement uncertainty. In the rare cases in which the individual measurements have significantly different uncertainties, a weighted mean should be adopted. For weighed mean, please refer to Part 4 – range image fusion, in which cases, weighted mean fusion is very popular.

Fusion of several time-series or spatial datasets can be seen as a series of fusion of single-value observations at each time or spatial point. Therefore, the condition in equation (4) also applies to the fusion of time-series and spatial data. Figure 2-1 illustrates a simple mean-based fusion of two noisy datasets acquired from a step profile. In this two dataset example, it can be observed that the simple mean provides efficient uncertainty reduction when individual datasets have equivalent uncertainties.

In some fusion situations, the measurement environment can manually be altered to obtain different results, which can compensate each other. For example, by altering the lighting conditions of a coherence scanning interferometer system, a sphere surface can give different measurement results [9], which are shown in Figure 2-2. The lower lighting result has valid sample data acquired in the relatively flat region, *i.e.* the sphere top and the base, but has missing data in the inclining regions, *i.e.* the sphere edges. In contrast, the higher intensity lighting result presents complementary data, *i.e.* more valid data in the inclining regions. A proper combination of the datasets can produce a result with a larger number of valid sample points, *i.e.* higher information completeness. Figure 2-2c presents such a fused result by pointwisely combining the two image datasets using the maximum sample value.

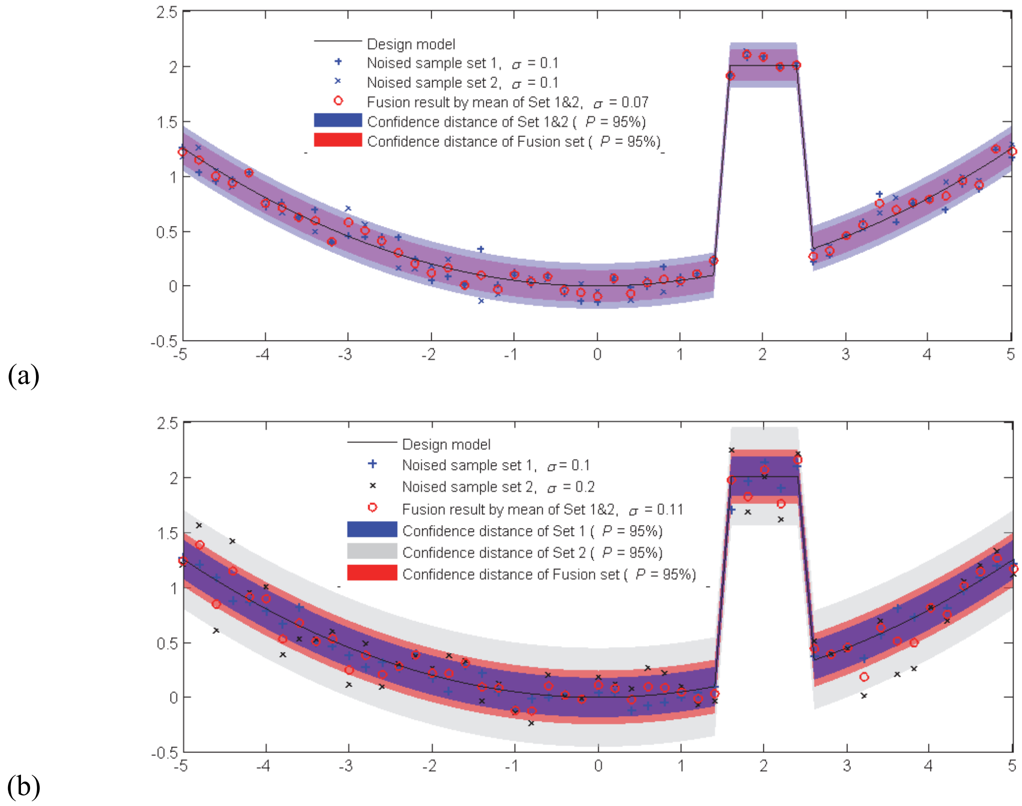

Figure 2-1. The uncertainties of the arithmetic mean fusion (a) decrease if two individual sets have similar uncertainties, (b) increase if an individual set has significantly lower uncertainty than the other.

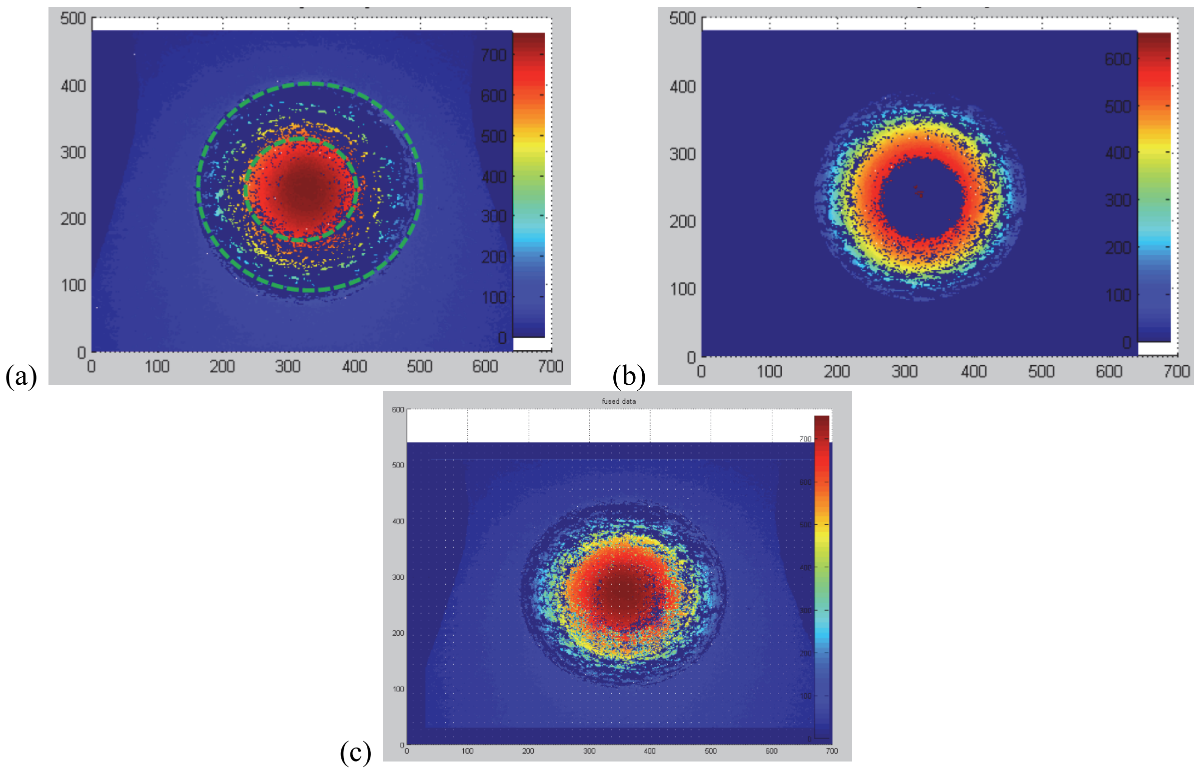

Figure 2-2. Different measurement results of a sphere surface under 25 % (a) and 35 % (b) light intensity setting, and (c) the fusion result [9].

3 STITCHING

3.1 INTRODUCTION

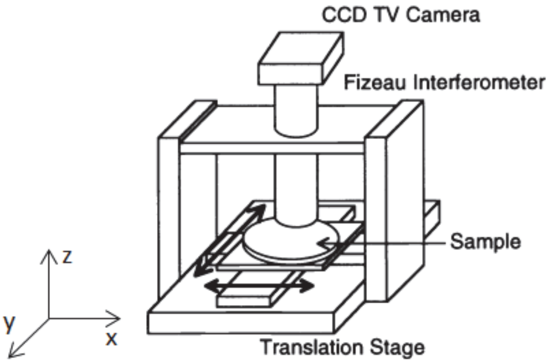

Figure 3-1. An example of sub-aperture stitching interferometer [17].

Stitching in surface topography measurement is the process of combining images from different sample areas using the same sensor and settings. Metrological stitching was initially proposed in sub-aperture interferometry measurement [17, 23]. In interferometry applications, a large area interferometer with a large aperture is usually not practical or cost effective; stitching of sub-aperture images to form a larger measuring area becomes a practical solution. Figure 3-1 is a schema of a typical stitching interferometer. Stitching techniques have been used for around two decades [17, 18, 24]. Stitching is also applicable to other areal measuring systems, for example AFM, confocal microscopy and focus variation systems.

Because the data to be fused in stitching is normally generated from the same sensor under the same settings [20], the sample points of two range images from neighbouring sample areas are naturally corresponding in a point-wise form. As in the case of repeated measurements, fusion of point-wisely corresponding data under the same settings can simply be achieved using an arithmetic mean [18]. Therefore, the core work of stitching is registration, which requires more intensive computation and sometimes instead, stitching is used to refer to just the registration process without the fusion process. In this report, stitching refers to the whole registration and fusion process.

Stitching requires a stage (see Figure 3-1) to control the lateral motion of the sample to an accuracy level below the image pixel width. In this way, neighbouring sub-aperture images can have an accurate positional relationship on the sampling plane and exact point-pair correspondence. Without a distinct point correspondence, fusion will be blind because one does not know with which sample point from a dataset should be combined for a sample point from another dataset.

Therefore, general registration deviations of a sub-aperture image have three main parameters in three dimensions, including tip/tilt (rotations around x-/ y-axes) and piston (translation in z-axis) [17]. There are advanced cases, such as stitching of spherical surfaces, in which geometrical deviations include higher order errors or off-axis errors, for example focus error, radial shift and clocking [18]. All the general and advanced stitching models can have the same expression

$$\boldsymbol{z}_{ref}(x, y) = \boldsymbol{z}(x, y) + \boldsymbol{\Phi}_{xy}\boldsymbol{\beta} + \boldsymbol{\varepsilon}, \tag{5}$$

where $\boldsymbol{\Phi}_{xy}$ is a stitching error modelling matrix, $\boldsymbol{\beta}$ is a vector of stitching parameters and $\boldsymbol{\varepsilon} \sim N(\mathbf{0}, \sigma^2 \boldsymbol{I})$. For a typical three-DoF stitching process [17], $\boldsymbol{\Phi}_{xy} = [\mathbf{1}, \boldsymbol{x}, \boldsymbol{y}]$ and $\boldsymbol{\beta} = [\beta_0, \beta_1, \beta_2]^{\mathrm{T}}$,

$$z_{ref}(x,y) = z(x,y) + \beta_0 + \beta_1 x + \beta_2 y + \varepsilon. \tag{6}$$

The main task of stitching algorithms is to find an optimised estimation of $\boldsymbol{\beta}$ for each individual sub-aperture dataset. There are different algorithms to estimate the stitching parameters $\boldsymbol{\beta}$ in which the least-squares estimation is usually preferred [17], and is presented below.

Given $\boldsymbol{K} = \{1,2,\dots,K\}$ sub-aperture images $\boldsymbol{z}_{k\epsilon\boldsymbol{K}}$, and by setting one as the reference, for example $\boldsymbol{z}_M$, estimation of the stitching parameters $\boldsymbol{\beta}_{k\epsilon\boldsymbol{K},k\neq M}$ becomes the following minimisation problem

$$\boldsymbol{\beta} = \operatorname{argmin} \sum_{i\epsilon\boldsymbol{K}} \sum_{j\epsilon\boldsymbol{K}} \left\| \boldsymbol{z}_{i\cap j} + \boldsymbol{\Phi}_{i\cap j}\boldsymbol{\beta}_i - \boldsymbol{z}_{j\cap i} - \boldsymbol{\Phi}_{j\cap i}\boldsymbol{\beta}_j \right\|_2^2 \tag{7}$$

where $\boldsymbol{\beta}_M = \mathbf{0}$, $\boldsymbol{\Phi}_{i\cap j} = \boldsymbol{\Phi}_{j\cap i}$, $\boldsymbol{z}_{i\cap j}$ denotes the z-data on the ith image, which corresponds to the jth image.

Let

$$\boldsymbol{P}_{i,j} = \boldsymbol{\Phi}_{i\cap j}^{\mathrm{T}}\left(\boldsymbol{z}_{i\cap j} - \boldsymbol{z}_{j\cap i}\right) = \begin{bmatrix} \sum_{i\cap j} \Delta z_{i,j} \\ \boldsymbol{x}_{i,j}^{\mathrm{T}} \Delta \boldsymbol{z}_{i,j} \\ \boldsymbol{y}_{i,j}^{\mathrm{T}} \Delta \boldsymbol{z}_{i,j} \end{bmatrix}, \tag{8}$$

$$\boldsymbol{Q}_{i,j} = \boldsymbol{\Phi}_{i\cap j}^{\mathrm{T}} \boldsymbol{\Phi}_{i\cap j} = \begin{bmatrix} n_{i,j} & \sum_{i\cap j} x_{i,j} & \sum_{i\cap j} y_{i,j} \\ \sum_{i\cap j} x_{i,j} & \boldsymbol{x}_{i,j}^{\mathrm{T}}\boldsymbol{x}_{i,j} & \boldsymbol{x}_{i,j}^{\mathrm{T}}\boldsymbol{y}_{i,j} \\ \sum_{i\cap j} y_{i,j} & \boldsymbol{y}_{i,j}^{\mathrm{T}}\boldsymbol{x}_{i,j} & \boldsymbol{y}_{i,j}^{\mathrm{T}}\boldsymbol{y}_{i,j} \end{bmatrix}, \boldsymbol{Q}_{i,i} = \mathbf{0}, \tag{9}$$

and

$$\boldsymbol{\beta}_i = \begin{bmatrix} \beta_{i,0} \\ \beta_{i,1} \\ \beta_{i,2} \end{bmatrix}, \tag{10}$$

the minimisation object function (equation (7)) has the solution which is obtained by letting the partial differential of $\boldsymbol{\beta}_j$ equal zero, *i.e.*

$$\begin{bmatrix} \sum_{j\epsilon\boldsymbol{K}} \boldsymbol{P}_{1,j} \\ \vdots \\ \sum_{j\epsilon\boldsymbol{K}} \boldsymbol{P}_{k,j} \\ \vdots \\ \sum_{j\epsilon\boldsymbol{K}} \boldsymbol{P}_{K,j} \end{bmatrix}_{k\neq M} = \begin{bmatrix} -\sum_{j\epsilon\boldsymbol{K}} \boldsymbol{Q}_{1,j} & \boldsymbol{Q}_{1,2} & \cdots & \boldsymbol{Q}_{1,K} \\ \boldsymbol{Q}_{2,1} & -\sum_{j\epsilon\boldsymbol{K}} \boldsymbol{Q}_{2,j} & \cdots & \boldsymbol{Q}_{2,K} \\ \vdots & \vdots & \ddots & \vdots \\ \boldsymbol{Q}_{K,1} & \boldsymbol{Q}_{K,2} & \cdots & -\sum_{j\epsilon\boldsymbol{K}} \boldsymbol{Q}_{K,j} \end{bmatrix} \begin{bmatrix} \boldsymbol{\beta}_1 \\ \vdots \\ \boldsymbol{\beta}_k \\ \vdots \\ \boldsymbol{\beta}_K \end{bmatrix}_{k\neq m}. \tag{11}$$

Once the sub-aperture images are registered, the sample data in the overlapping areas of two sub-aperture measurements can be combined using simple means, *i.e.*

$$\boldsymbol{z}_{fused}(x,y) = \operatorname{mean}\left\{\boldsymbol{z}_{ref}(x,y),\ \boldsymbol{z}(x,y) + \boldsymbol{\Phi}_{xy}\boldsymbol{\beta}\right\}. \tag{12}$$

An alternative stitching algorithm exists which stitches neighbouring sub-aperture data in a sequence. This algorithm locally computes the stitching parameter vector $\boldsymbol{\beta}_i$ for each dataset by referencing it to the registered datasets, for example the j^{th} set, which have overlapping sample points, via the linear system,

$$\boldsymbol{P}_{i,j} = -\boldsymbol{Q}_{i,j}\boldsymbol{\beta}_i. \tag{13}$$

However, the sequential stitching algorithm has been claimed to produce accumulative stitching error and is, therefore, not recommended [17, 24].

In practice, the stitching solutions mentioned above rely on a high-accuracy lateral motion stage. If an inadequate motion stage is applied, additional control errors, for example the translational error on x- and y-directions, and the rotation error in z-axis, contribute significantly to the stitching result. For the measurement of non-planar surfaces, the additional error induced by crude work motion stages needs extra concerns. For example, an affine transformation registration (x- and y-coordinates only) of sub-aperture measurements is initially applied before the stitching [24].

In generalised stitching applications, in which the datasets to be fused are not grid images or the images have variable sampling intervals, there is usually no point-pair correspondence between neighbouring datasets. Point-pair correspondence needs to be analysed before the implementation of the stitching algorithms in equation (11). A closest point iterative stitching, or so-called sub-aperture stitching and localisation (SASL) [25, 26], has been developed recently to solve the generalised stitching problem. SASL iteratively finds the closest point correspondence between each sub-aperture dataset and a stitching algorithm is carried out. SASL is a successful extension of the typical stitching algorithm in equation (11).

Stitching accuracy is also influenced by the size of overlapping areas. The larger the overlapping area a dataset has with its neighbouring datasets, the higher-accuracy stitching it can achieve, because more sample points are taken for optimising calculations. It has been demonstrated [17] that control of the overlapping width above thirteen pixels ensures the stitching error at the far end pixel positions is below the standard deviation of the individual pixel values for 128 × 128 images.

3.2 EXAMPLES

Figure 3-2 shows two sub-aperture measurements (1024 × 1024) of a structured surface using a CSI system. The two range images have about 20 % (≈ 150 pixels in width) overlapping areas. Applying the least-squares stitching algorithm of equation (11), by setting Figure 3-2a as the reference, the stitched result is shown in Figure 3-2c. It can be noticed that the data in Figure 2-5b was tilted (the righ-hand pixels have colour downgraded from red to yellow) and the stitched result has visually smooth performance in the overlapping area.

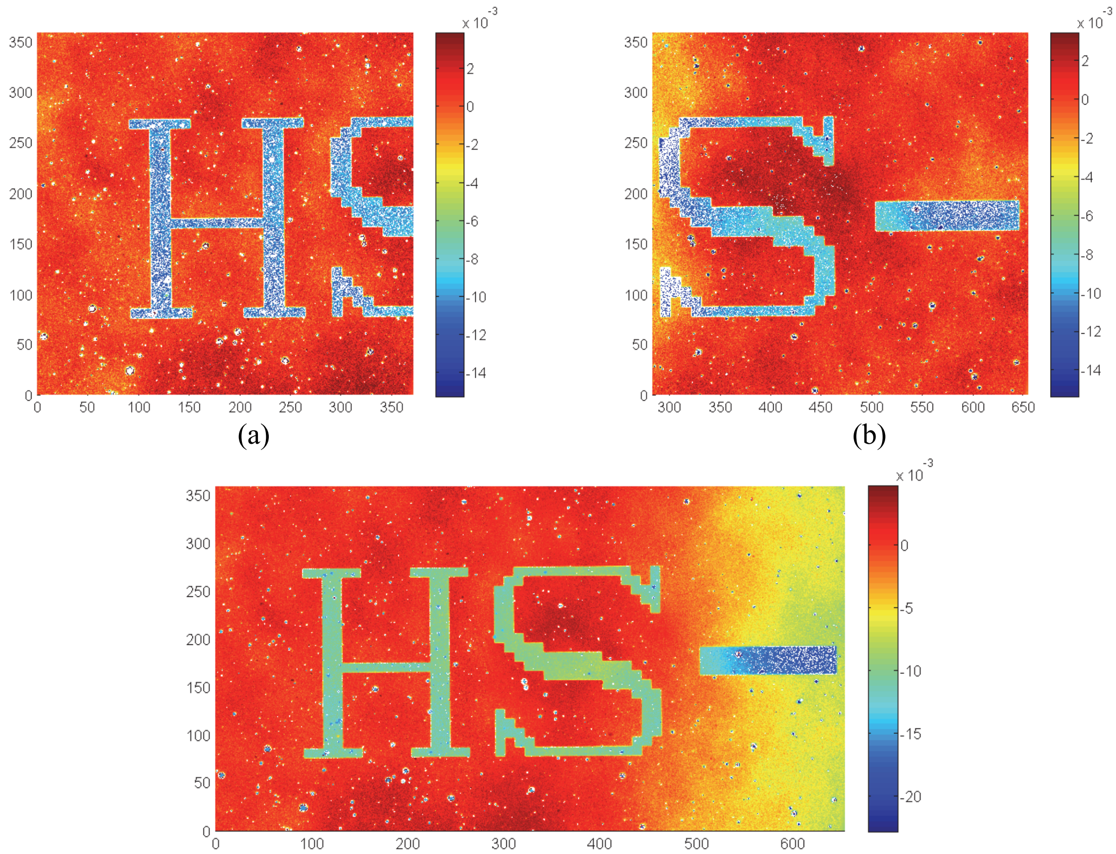

(c)

Figure 3-2. Two sub-aperture measurements (a) and (b) from a CSI and the stitching result (c), units in micrometres.

The same procedures were implemented for nine sub-aperture measurements of a MEMS chip [27] shown in Figure 3-3. By setting Figure 3-3g as the reference, the least-squares stitching result is presented in Figure 3-3j.

The two examples show that the typical least-squares stitching algorithm in equation (11) can work successfully for structured surfaces. A quantitative evaluation of the stitching accuracy of the algorithm is not given because there are no appropriate experimental conditions.

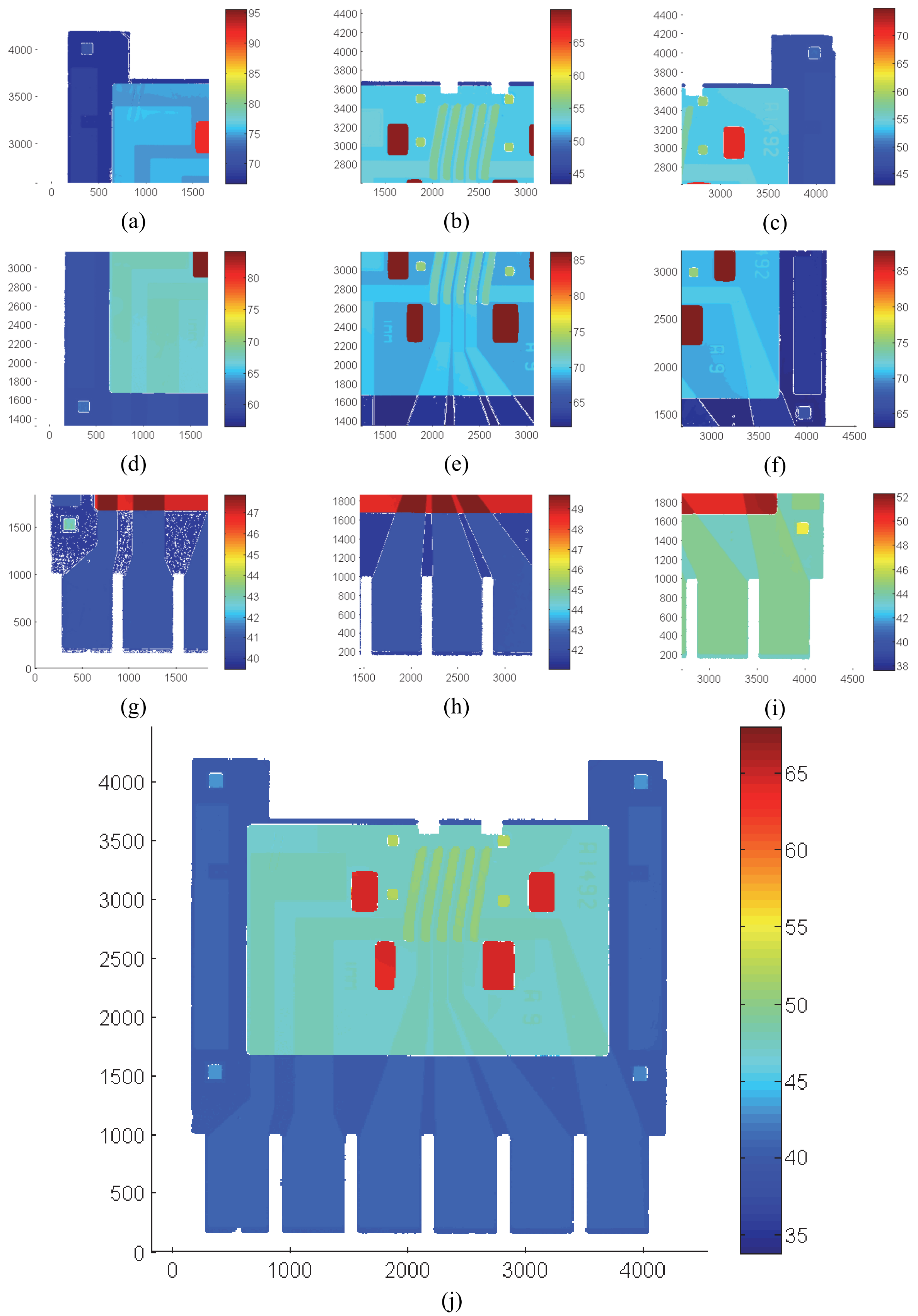

Figure 3-3. Nine sub-aperture measurements (a – i) and the stitched result (j), units in micrometres (note the *z*-scale change of each sub-image before and after the fusion).

4 RANGE IMAGE FUSION

Range image fusion is an extension of stitching. The datasets to be fused in range image fusion do not need to be homogeneous, *i.e.* from the same sensor and the same settings. Range images to be fused can be from the same instrument with different objectives or sample settings, or from different instruments. Because there is no natural point-pair correspondence between overlapping datasets, a cross-resolution image registration algorithm and fusion algorithm need to be used.

Resampling is a popular solution to prepare inhomogeneous datasets to be fused with the same sampling conditions before data fusion. Once resampling is completed, a two-step registration method is carried out [28]. A coarse matching, based on the sum of absolute differences (SAD) or normalised cross correlation (NCC), is initially conducted [28] to register the datasets with x- and y-translations. The stitching algorithm in equation (11) is then used to refine the registration in another three dimensions, including x-/y- rotations and z-translation. The two-step registration in a total of five DoFs has been successfully used in advanced stitching techniques [24]. A full 6-DoF registration may not be necessary for areal measurement in which sample stages with high rotational stability around the z-axis are normally available. Ramasamy's research [9] introduced a full 6-DoF registration process for range image fusion which needed sophisticated data manipulation and intensive computation.

In the fusion process, because input datasets with different resolutions usually have different uncertainty and information richness (measurement bandwidths), a weighted mean is normally taken on the resampled datasets [9]. *Via* a weighted mean, the uncertainty of the fusion results can be expected to be reduced. However, the weights usually need to be appropriately designed so the fused result has improved accuracy.

Now, the process to obtain the optimal weights is shown below. Assume two sensors have acquired sample data y_1 and y_2 at a common location, with different standard uncertainty, σ_1 and σ_2. A weighted mean fusion of the individual results

$$y_F = a_1 y_1 + a_2 y_2, \text{ s.t. } (a_1 + a_2 = 1) \tag{14}$$

is expected to have the minimum standard uncertainty with well-designed weights, where a_i are the weights, *i.e.* to solve the minimisation problem

$$P_2\text{: argmin}\, \sigma_F^2 = a_1^2\sigma_1^2 + a_2^2\sigma_2^2, \text{ s.t. } a_1 + a_2 = 1, 0 \le a_i \le 1. \tag{15}$$

The optimal weights can be easily solved for the simple two sensor fusion case as

$$\begin{aligned} a_1 &= \frac{\sigma_2^2}{\sigma_1^2+\sigma_2^2} \\ a_2 &= \frac{\sigma_1^2}{\sigma_1^2+\sigma_2^2} \end{aligned}. \tag{16}$$

The fusion output y_F hence has the reduced standard uncertainty

$$\min \sigma_F = \frac{\sigma_1\sigma_2}{\sqrt{\sigma_1^2+\sigma_2^2}}. \tag{17}$$

If more than two results are fused and the individual results have standard measurement uncertainties $\sigma_1, \sigma_2, \dots, \sigma_n$, the optimisation problem for the weights $a_1, a_2, \dots, a_n$ can be written as

$$P_n: \operatorname{argmin}_{\boldsymbol{a}} \sigma_F^2 = \boldsymbol{a}^{\mathrm{T}}\boldsymbol{\Sigma}^2\boldsymbol{a}, \text{ s.t. } \boldsymbol{u}^{\mathrm{T}}\boldsymbol{a} = 1, \boldsymbol{a} \in [0,1]_n, \tag{18}$$

where $\boldsymbol{a} = [a_1, a_2, \dots, a_n]^{\mathrm{T}}$, $\boldsymbol{\Sigma} = \operatorname{diag}(\sigma_1^2, \sigma_2^2, \dots, \sigma_n^2)$ and $\boldsymbol{u} = [1,1, \dots, 1]_n^{\mathrm{T}}$.

The equality constrained minimisation problem in equation (18) can be converted to its Lagrange form,

$$P_{n+1}: \operatorname{argmin}_{\boldsymbol{a},\lambda} \sigma_F^2 = \boldsymbol{a}^{\mathrm{T}}\boldsymbol{\Sigma}^2\boldsymbol{a} + \lambda\left(\boldsymbol{u}^{\mathrm{T}}\boldsymbol{a} - 1\right), \boldsymbol{a} \in [0,1]_n, \tag{19}$$

which can easily be solved by solving the following linear system

$$\begin{bmatrix} \boldsymbol{\Sigma}^2 & \boldsymbol{u} \\ \boldsymbol{u}^{\mathrm{T}} & 0 \end{bmatrix} \begin{bmatrix} \boldsymbol{a} \\ \lambda \end{bmatrix} = \begin{bmatrix} \boldsymbol{0} \\ 1 \end{bmatrix}. \tag{20}$$

Therefore, the optimised weights for the individual results are

$$a_i = \frac{1}{\sigma_i^2 \sum \frac{1}{\sigma^2}}, i = 1,2, \dots, n. \tag{21}$$

With the optimised weights to choose, the fusion using equation (14) can always provide fusion outputs with a reduced uncertainty. In the optimised situation, the fused result has the minimum standard uncertainty which is smaller than the uncertainty σ_i of each individual result:

$$\min \sigma_F^2 = \frac{1}{\sum \frac{1}{\sigma^2}}. \tag{22}$$

In practical measurement, however, the measurement uncertainties of the individual results are usually unknown or inaccurate, which indicates the weight design using equation (21) is usually not available. Alternative weight designs have been introduced from image processes which provide approximate solutions as above, including the regional energy (RE) [29], regional edge intensity (REI) [30] and the combination of wavelet coefficients and local gradients (WGC) [31]. However, weak evidence on the reliability of the compromising solutions has been found. The uncertainty propagation, based on the compromising weighting methods, is currently unknown. For more details about the weight designs for range image fusion, please refer to reference [9].

5 3D DATA FUSION

5.1 INTRODUCTION

In this report, 3DDF refers to the fusion of 3D spatial datasets. In 3DDF, the datasets to be fused can be 3D point clouds or a mix of 3D point clouds with 2.5D range images. In other words, 3DDF is an extension of stitching and range image fusion, but designed for more complex situations. 2.5D here means that measured datasets have three dimensions in total in which one-dimensional data is a function of the other two-dimensional data. 2.5D data cannot describe geometry with re-entrant features [32], while 3D data can represent geometry with arbitrary shape.

3DDF is increasingly becoming an engineering solution for advanced measurement of surface geometry. For example, full measurement of an object can usually be accomplished by several local or global measurements of the top surfaces at different areas around the object followed by data fusion.

Figure 5-1 presents the main procedures of a 3DDF-based surface measurement. First, the surface of an object is divided into segments and independently measured. Because individual measurements are independent, the coordinate systems of the individual datasets are different. Registration of the datasets into a common coordinate system is then carried out to enable the fusibility of the datasets (see Figure 5-1b). The registration process normally needs individual measurements covering common fiducial marks or signatures to improve registration accuracy. The data fusion process occurs in the third step in which the redundant or inconsistent data in the overlapping areas of independent measurements are combined for a unified output.

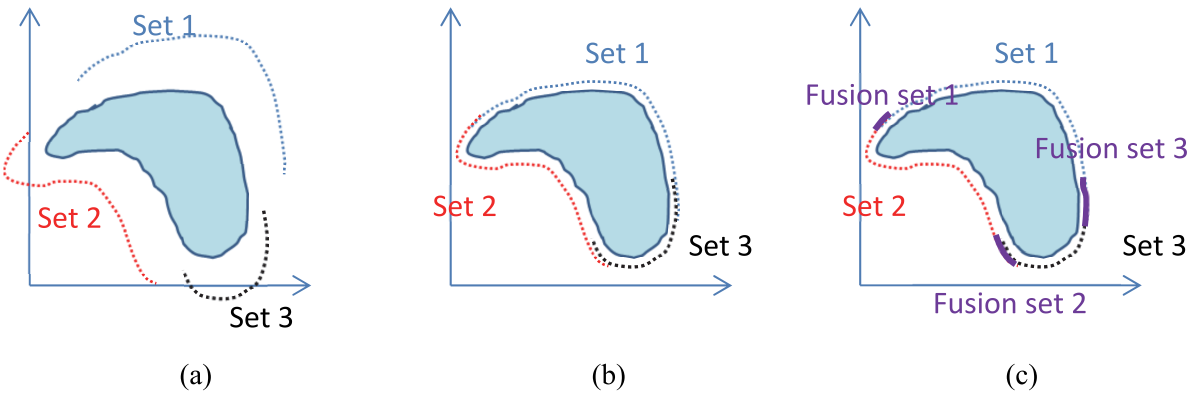

Figure 5-1. Illustration of the main processes in 3DDF-based surface measurement. Step 1 (a) obtains independent surface measurement at local areas; Step 2 (b) registers the local sets into a common coordinate system; Step 3 (c) implements fusion process for the data in overlapping areas.

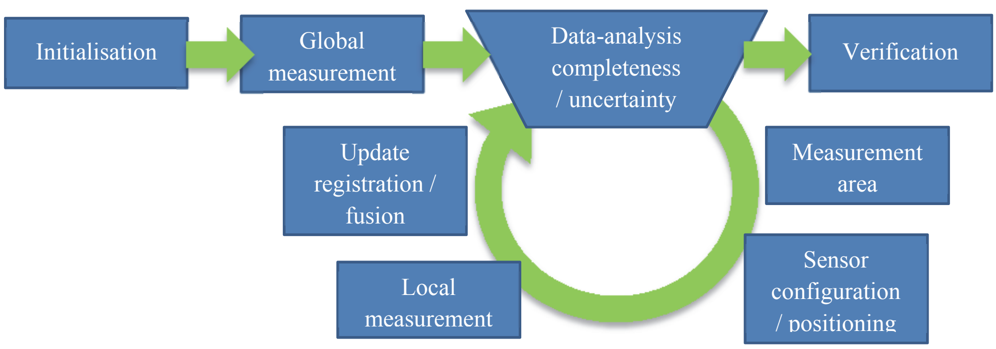

Figure 5-2. A multi-scale data fusion–based measurement framework [11].

In most of cases, 3DDF tackles datasets on different scales, *i.e.* the datasets to be fused have different measuring ranges, sample positions and sample densities. The 3DDF problem and relative solutions for datasets on different scales are also referred to as multi-scale data fusion [11]. A typical multi-scale data fusion-based measurement framework is shown in Figure 5-2. For example, a CMM or computer tomography (CT) system is used to obtain a global description of an object with a low-density point set. High density CSI measurement data at local areas can then be integrated in to increase the information richness. A combination of CMM or CT, and CSI datasets can produce industrially useable measurement results [11].

3DDF requires more complex data process techniques than in the previous cases. For example, registration of two 3D datasets should be carried out on a point cloud basis, instead of a range image basis. Registration with full 6-DoFs (three translational and three rotational) is usually necessary because spatial point cloud data is often obtained with equivalent measuring accuracy in all the three Cartesian dimensions.

Fusion of 3D data in all three dimensions is usually avoided because it requires three times the computation cost for each dimension. Most existing 3DDF algorithms simplify the fusion of 3D data into a 1D problem by using the other 2D data as arguments. For example, 3D data is projected on a reference surface to form a set of scattered points without under-cuts, *i.e.* the surface height z is a function of the arguments x and y: $z = f(x, y)$. In this way, a 3DDF problem can be simplified into 1D fusion solely for z-data.

5.2 FUSION METHODS

3DDF methods can be classified into two types: parametric modelling-based weighted fusion methods and non-parametric modelling-based methods.

Parametric weighting methods approximate source signals using a linear model in which the model parameters are obtained *via* a weighting method. The parametric fusion solutions include weighted least-squares fusion and Kalman filter fusion. Once the model parameters are obtained, fusion results are determined.

Non-parametric methods train a non-parametric model to approximate source signals and the fusion results are obtained based on the trained model and a combination with input data. The surface model is non-parametric, which means the model hyper-parameters cannot determine the fusion output without the assistance of input data. Typical non-parametric fusion methods include Gaussian process (GP) fusion methods, which approximate the difference of two measurement signals using a GP.

5.2.1 Weighted least-squares fusion

Weighted least-squares (WLS) fusion [12, 33] is a well-developed method, the applications of which are limited at present. WLS fusion relies on an optimised linear approximation of surface geometry with added Gaussian noise [12, 34] *i.e.*

$$\boldsymbol{y} = \boldsymbol{C}\boldsymbol{\alpha} + \boldsymbol{\varepsilon} \tag{23}$$

where $\boldsymbol{y}$ is a size n column vector of the observed sample values, $\boldsymbol{\alpha}$ is a size m column vector whose entries correspond to the unknown parameters of a model, $\boldsymbol{C}$ is a n by m model basis function matrix (sometimes called a design matrix), which is determined by the parametric model, and $\boldsymbol{\varepsilon}$ is a size n noise column vector which has the entries $\varepsilon_i \sim \mathbb{N}(0, \sigma^2)$.

For 2.5D scattered surface samples, equation (23) has the form

$$\boldsymbol{z} = \boldsymbol{C}(\boldsymbol{x}, \boldsymbol{y})\boldsymbol{\alpha} + \boldsymbol{\varepsilon}. \tag{24}$$

For example, if modelling a surface using a simple 1st degree plane, *i.e.* $z = \alpha_1 x + \alpha_2 y + \alpha_3$, the design matrix $\boldsymbol{C} = [\boldsymbol{x}, \mathbf{y}, \mathbf{1}]$ with $\boldsymbol{\alpha} = [\alpha_1, \alpha_2, \alpha_3]^{\mathrm{T}}$.

Given K datasets from different instruments or sensors $\boldsymbol{z}_k(x_i, y_i)_{i\in I_k, k\in K}$, a simple linear fusion system can be constructed [34] as

$$\begin{bmatrix} \boldsymbol{z}_1 \\ \boldsymbol{z}_2 \\ \vdots \\ \boldsymbol{z}_K \end{bmatrix} = \begin{bmatrix} \boldsymbol{C}_1 \\ \boldsymbol{C}_2 \\ \vdots \\ \boldsymbol{C}_K \end{bmatrix} \boldsymbol{\alpha} + \begin{bmatrix} \boldsymbol{\varepsilon}_1 \\ \boldsymbol{\varepsilon}_2 \\ \vdots \\ \boldsymbol{\varepsilon}_K \end{bmatrix}, \tag{25}$$

where $\boldsymbol{C_i}$ is the design matrix for each dataset, $\boldsymbol{\varepsilon}_i \sim \mathbb{N}(\boldsymbol{0}, \sigma_i^2 \boldsymbol{I})$. A best linear unbiased estimation (BLUE) of the model parameters $\boldsymbol{\alpha}$ can be achieved by minimising the objective function

$$\operatorname{argmin}_{\boldsymbol{\alpha}} \sum w_i (\boldsymbol{z}_i - \boldsymbol{C}_i\boldsymbol{\alpha})^{\mathrm{T}} (\boldsymbol{z}_i - \boldsymbol{C}_i\boldsymbol{\alpha}), \tag{26}$$

provided $w_i = \frac{1}{\sigma_i^2}$. The minimisation can be achieved by restricting the partial differential with respect to $\boldsymbol{\alpha}$ to $\boldsymbol{0}$, *i.e.*

$$\sum \boldsymbol{C}_i{}^{\mathrm{T}} \boldsymbol{W}_i \boldsymbol{C}_i \boldsymbol{\alpha}_F = \sum \boldsymbol{C}_i{}^{\mathrm{T}} \boldsymbol{W}_i \boldsymbol{z}_i, \tag{27}$$

where $\boldsymbol{W}_i = \mathrm{diag}(w_i, \dots, w_i)$. Equation (27) can be further written as

$$\boldsymbol{C}^{\mathrm{T}} \boldsymbol{W} \boldsymbol{C} \boldsymbol{\alpha}_F = \boldsymbol{C}^{\mathrm{T}} \boldsymbol{W} \boldsymbol{z}, \tag{28}$$

where $\boldsymbol{C}^{\mathrm{T}} = [\boldsymbol{C}_1^{\mathrm{T}}, \boldsymbol{C}_{\boldsymbol{2}}^{\mathrm{T}}, \dots, \boldsymbol{C}_k^{\mathrm{T}}]$, $\boldsymbol{W} = \mathrm{diag}(\boldsymbol{W}_1, \boldsymbol{W}_2, \dots, \boldsymbol{W}_K)$ and $\boldsymbol{z} = [\boldsymbol{z}_1^{\mathrm{T}}, \boldsymbol{z}_2^{\mathrm{T}}, \dots, \boldsymbol{z}_{\boldsymbol{K}}^{\mathrm{T}}]^{\mathrm{T}}$.

Therefore, the weighted least-square fusion estimation of the model parameter $\boldsymbol{\alpha}$ has the form

$$\boldsymbol{\alpha}_F = \left(\boldsymbol{C}^{\mathrm{T}} \boldsymbol{W} \boldsymbol{C}\right)^{-1} \boldsymbol{C}^{\mathrm{T}} \boldsymbol{W} \boldsymbol{z}. \tag{29}$$

In the special case when $\boldsymbol{C_i} = \boldsymbol{I}$, *i.e.* $\boldsymbol{z} = \boldsymbol{\alpha} + \boldsymbol{\epsilon}$, equation (29) can be written as

$$\boldsymbol{z_F}|_{\boldsymbol{C}_i = \boldsymbol{I}} = \left(\sum \boldsymbol{W}_i\right)^{-1} \sum (\boldsymbol{W}_i \boldsymbol{z}_i). \tag{30}$$

For example, in the fusion of two range images acquired at the same sampling positions, the two same size datasets can be directly weighted according to equation (30) without an approximate model.

Figure 5-3 presents an example of the fusion of two uncertainty-differing datasets from a quadratic curve. Based on 2000 simulations with added random noise, the weighted fusion results steadily show a reduction of the standard variance by about 1/6 from the lowest individual set. Figure 5-4 presents another example of the fusion of two uncertainty-differing datasets from a B-spline curve with knots set at $[-0.5, -0.4, 0, 0.4, 0.6]$. 2000 simulations with added random noise show a steady standard variance reduction by about 1/10 from the lowest individual set. In both of the examples, non-weighted fusion results were also calculated by setting the weights $w_1 = w_2 = 1$. This shows that non-weighted fusion only works effectively for datasets with similar uncertainty levels, which is consistent with the weighted fusion solutions in Section 4.

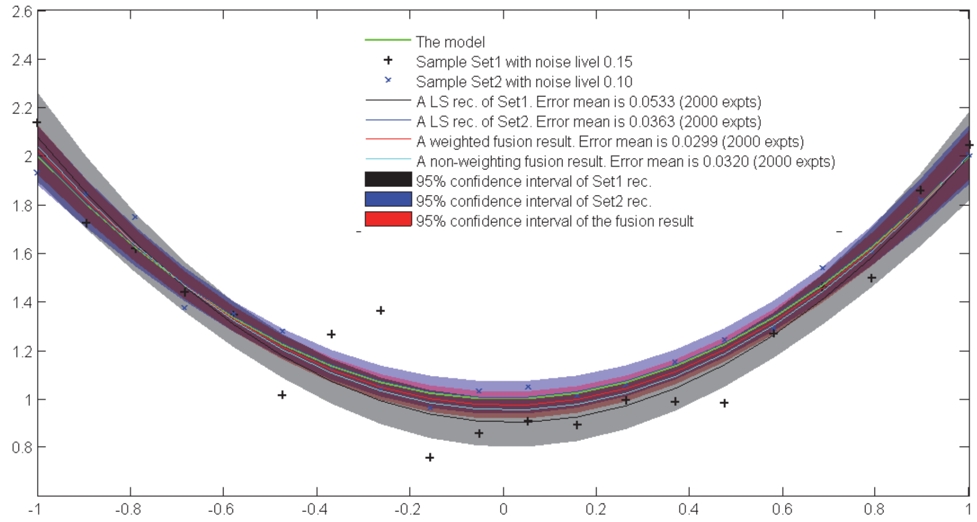

Figure 5-3. A fusion example of noisy data from a quadratic curve.

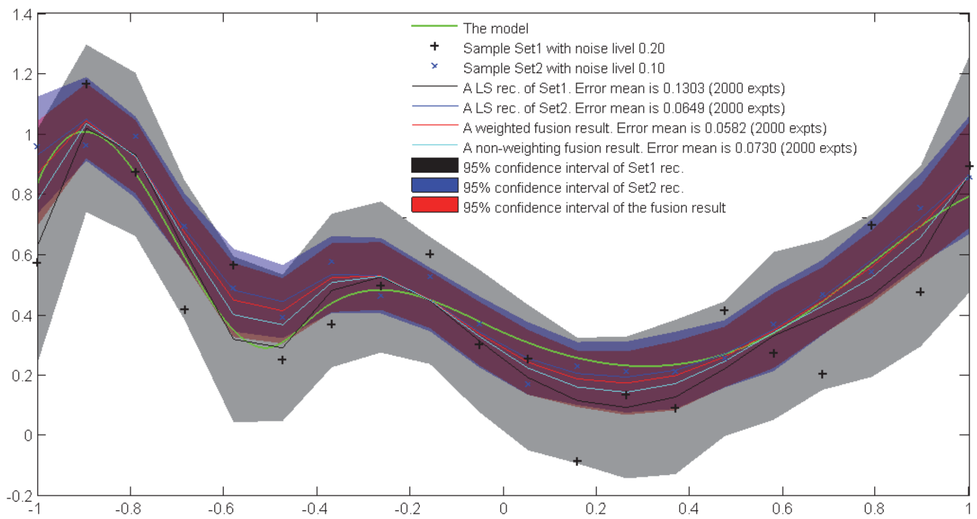

Figure 5-4. A fusion example of noisy data from a B-spline curve.

For structured surfaces or freeform surfaces with sharp geometrical changes, the fitting accuracy using linear modelling methods is usually problematic, though the validity of a model can be examined [35]. For example, a B-spline model with less parameters or improper knot setting cannot model a structured signal appropriately; a complex model with too many parameters will run into the danger of overfitting [36]. For multi-dimensional problems, tensor-product methods with linear modelling are popular solutions which, however, have been known to be deficient for non-tensor-product geometries, for example a circle feature. Tensor product methods are also regarded as not appropriate for complex geometries. For example, a smooth surface embedded by sharp features along its diagonal line [36] requires dense B-spline knot settings on both lateral directions, which is computational wasteful.

5.2.2 Kalman filter fusion

The Kalman filter (KF) was first proposed by Kalman in 1960 [37]. It is a method to estimate the internal state of a dynamical system through sequentially observing an external measurand [38]. Given a time-dependent system with its linear model related to the internal state and the external observations, the KF uses conventional Bayesian statistics to estimate the posterior distributions of the internal state based on the current and previous observations, through [1]

$$p(\boldsymbol{x}_k, \boldsymbol{z}_k | \boldsymbol{z}_{k-}) = p(\boldsymbol{x}_k | \boldsymbol{z}_k) p(\boldsymbol{z}_k | \boldsymbol{z}_{k-}) = p(\boldsymbol{z}_k | \boldsymbol{x}_k) p(\boldsymbol{x}_k | \boldsymbol{z}_{k-}) \tag{31}$$

where $\boldsymbol{x}_k$ is the k^{th} internal state variable to be estimated, $\boldsymbol{z}_k$ is the k^{th} observed external measurand, $\boldsymbol{z}_{k-}$ denotes all previously observed measurands before the k^{th}, *i.e.* $\boldsymbol{z}_{k-} = \{\boldsymbol{z}_1, \boldsymbol{z}_2, ..\boldsymbol{z}_{k-1}\}$, $p(\boldsymbol{x}_k | \boldsymbol{z}_{k-})$ is the prior probability density function (pdf) based on previous observations, $p(\boldsymbol{z}_k | \boldsymbol{x}_k)$ is the likelihood function and $p(\boldsymbol{z}_k | \boldsymbol{z}_{k-})$ is the conditional probability density of the occurrence of the k^{th} observations. Hence, the posterior distribution $p(\boldsymbol{x}_k, \boldsymbol{z}_k | \boldsymbol{z}_{k-})$ at each time can be recursively updated when newer datasets are integrated.

The KF predicts the posterior distribution of $\widehat{\boldsymbol{x}}_k$ based on a prior estimation $\widehat{\boldsymbol{x}}_{k-}$ and a current observation $\boldsymbol{z}_k$, which can be written in the form

$$\widehat{\boldsymbol{x}}_k = \widehat{\boldsymbol{x}}_{k-1} + \boldsymbol{K}_k (\boldsymbol{z}_k - \boldsymbol{H}_k \widehat{\boldsymbol{x}}_{k-1}) \tag{32}$$

where $\boldsymbol{K}_k$ is called Kalman gain, $\boldsymbol{H}_k$ is the measurement matrix in the k^{th} observation, which has the linear Gaussian form

$$\boldsymbol{z}_k = \boldsymbol{H}_k \widehat{\boldsymbol{x}}_k + \boldsymbol{\epsilon}, \ \boldsymbol{\epsilon} \sim N(\boldsymbol{0}, \sigma^2 \boldsymbol{I}). \tag{33}$$

If the measurement system is constant among different measurements, then $\boldsymbol{H}_k = \boldsymbol{H}_{k+1}$. The item $\boldsymbol{z}_k - \boldsymbol{H}_k \widehat{\boldsymbol{x}}_{k-1}$ in equation (32) is the prediction residual, found by subtracting the current observation from the predicted measurement based on previous measurements. To ensure $\widehat{\boldsymbol{x}}_k$ has the minimum prediction residual, *i.e.* $tr(E[(\widehat{\boldsymbol{x}}_k - \boldsymbol{x}_k)(\widehat{\boldsymbol{x}}_k - \boldsymbol{x}_k)^T])$, the optimal Kalman gain [38] should have the following form

$$\boldsymbol{K}_k = \boldsymbol{V}_{\widehat{\boldsymbol{x}}_{k-1}} \boldsymbol{H}_k{}^T \left(\boldsymbol{H}_k \boldsymbol{V}_{\widehat{\boldsymbol{x}}_{k-1}} \boldsymbol{H}_k{}^T + \boldsymbol{V}_{\boldsymbol{z}_k}\right)^{-1} \tag{34}$$

where $\boldsymbol{V}_{\boldsymbol{z}_k}$ and $\boldsymbol{V}_{\widehat{\boldsymbol{x}}_{k-1}}$ are respectively the variance (square) matrix of the k^{th} observation and the (k-1)th prediction. With equation (34), it can be shown that

$$\boldsymbol{V}_{\widehat{\boldsymbol{x}}_k} = (\boldsymbol{I} - \boldsymbol{K}_k \boldsymbol{H}_k) \boldsymbol{V}_{\widehat{\boldsymbol{x}}_{k-1}}. \tag{35}$$

From equation (34), it can be shown that, when the current measurement noise is extremely low, *i.e.* $\boldsymbol{V}_{\boldsymbol{z}_k} \to \boldsymbol{0}$, then $\boldsymbol{K}_k \to \boldsymbol{H}_k{}^{-1}$ [39], which means $\widehat{\boldsymbol{x}}_k$ is mainly determined by $\boldsymbol{z}_k$ because it is highly reliable. If a prior estimation has the variance $\boldsymbol{V}_{\widehat{\boldsymbol{x}}_{k-1}}$ approaching zero, $\boldsymbol{K}_k$ approaches zero. In this situation, $\widehat{\boldsymbol{x}}_k$ is mainly determined by the previous estimation $\widehat{\boldsymbol{x}}_{k-1}$.

With equations (32) to (35), the estimation of the system parameters can be recursively updated. Or alternatively, the final estimation can be obtained using a batch mode [33]:

$$\widehat{\boldsymbol{x}}_k = \left(\boldsymbol{V}_{\boldsymbol{x}_0}^{-1} + \boldsymbol{H}^T\boldsymbol{V}_{\boldsymbol{z}}\boldsymbol{H}\right)^{-1}\left(\boldsymbol{V}_{\boldsymbol{x}_0}^{-1}\boldsymbol{x}_0 + \boldsymbol{H}^T\boldsymbol{V}_{\boldsymbol{z}}\boldsymbol{z}\right) \tag{36}$$

where $\boldsymbol{H}^T = \left[\boldsymbol{H}_1^T, \boldsymbol{H}_2^T, \ldots, \boldsymbol{H}_k^T\right]$, $\boldsymbol{V}_{\boldsymbol{z}}^{-1} = \mathrm{diag}\left(\boldsymbol{V}_{\boldsymbol{z}_1}^{-1}, \boldsymbol{V}_{\boldsymbol{z}_2}^{-1}, \ldots, \boldsymbol{V}_{\boldsymbol{z}_k}^{-1}\right)$ and $\boldsymbol{z} = \left[\boldsymbol{z}_1^T, \boldsymbol{z}_2^T, \ldots, \boldsymbol{z}_k^T\right]^T$. It can be shown that, if $\boldsymbol{V}_{\boldsymbol{x}_0}$ is infinitely large and $\boldsymbol{x}_0$ is zero or a finite constant, then equation (36) is simplified to the WLS fusion equation (29), where $\boldsymbol{W} = \boldsymbol{V}_{\boldsymbol{z}}^{-1}$. In practical computations, $\boldsymbol{x}_0$ is normally set as $\boldsymbol{0}$ and $\left\|\boldsymbol{V}_{\boldsymbol{x}_0}\right\| = +\infty$, which means the Kalman filter fusion and the weighted least-squares fusion are essentially equal.

Compared to WLS fusion, the advantage of KF fusion is that it can be sequentially applied to new datasets without the knowledge of every previous measurement. This is very useful when there are a lot of datasets to be fused and significantly saves computational storage.

Since KF fusion and WLS have essentially the same fusion output, more details of KF are not given in this report. An application of KF in the fusion of surface metrological data can be found in reference [33].

5.2.3 Gaussian process fusion

Compared to parametric modelling, non-parametric modelling is a significant improvement which can approximate sharp-change geometry well or for non-tensor-product geometry. Non-parametric statistical models have been introduced to data fusion for their high flexibility in fitting, and machine learning [40]. Gaussian process (GP) fusion models [41, 42], also widely referred to as GP linkage models, with maximum marginal likelihood estimation, have recently being applied to spatial data in dimensional metrology [8, 10]. With GP fusion, the hyper-parameters of a GP fusion model, which describe the mean function and covariance function of the model, are first estimated *via* a Bayesian inference [40]. The hyper-parameters with initial input data are then used to estimate the fusion results. GP fusion [8, 10, 41] has been successfully demonstrated for the improvement of measurement reliability.

An effective implementation of GP fusion usually requires that input datasets have different reliability or fidelity levels, *i.e.* uncertainty. If there is no difference in the uncertainty for input datasets [42], the performance of GP fusion may be uncertain. In addition, GP fusion tackles only two sets of data as inputs for a computation, which means that fusion of multiple datasets requires iterative fusion computations for each dataset with previous fusion output, as with KF fusion.

There are several GP fusion sub-models, all of which construct a GP function to approximate the residuals between two input datasets. Given two datasets, with one as the high reliability (HR) set z_1 and the other as the low reliability (LR) set z_2, GP fusion links the two datasets by approximating the residuals as a GP function. For example, a typical fusion model is expressed as

$$\begin{gathered} z_1(x_i, y_i) = \beta(x_i, y_i)\hat{z}_2(x_i, y_i) + \delta(x_i, y_i) + \varepsilon_1, \varepsilon_1 \sim N(0, \sigma_1^2), \\ z_2(x_i, y_i) = \hat{z}_2(x_i, y_i) + \varepsilon_2, \varepsilon_2 \sim N(0, \sigma_2^2), \\ \beta(x_i, y_i) = \beta_0 + \beta_1 x_i + \beta_2 y_i, \\ \delta \sim GP\left(m_r, k_{l_r, \sigma_r^2}\right), \end{gathered} \tag{37}$$

where $\hat{z}_2$ is a fitted (or denoised) version of the LR set z_2 with $\hat{z}_2 \cong z_2$, δ, defined by the mean function m_r and the covariance function k_{l_r,σ_r^2} is the GP linkage function which describes the systematic offset between the two input datasets, β is a rescaling function dependent on x and y, and ε_1 and ε_2 are white noise. β can be substituted by other polynomial functions. However, it has been claimed [8] that simple 1st degree polynomial rescaling is flexible enough for most practical cases. β can simply be set as 1 if there is no scale bias between z_1 and z_2. Based on the linkage model in equation (37), the fusion result can be expressed by a composition of the denoised LR data plus the GP linkage function, which describes the residuals between the two inputs:

$$z_F = \beta(x_i, y_i)\hat{z}_2(x_i, y_i) + \delta(x_i, y_i). \tag{38}$$

GP fusion has many sub-methods depending on the constructions of different $\hat{z}_2$. For example, $\hat{z}_2$ can be another GP model with $\mathbf{0}$ as the mean, *i.e.*

$$\hat{z}_2(x_i, y_i) \sim GP\left(\mathbf{0}, k_{l_2,\sigma_2^2}\right). \tag{39}$$

The $\mathbf{0}$-mean GP model can provide an optimised approximation for smooth signals. If the source signal has a non-$\mathbf{0}$ form, the $\mathbf{0}$-mean can be replaced by other simple polynomial functions [42]. By combining the models in equations (39) and (37), which individually approximate an input and the residuals of it from another input, a hierarchical GP model can be constructed. The hierarchical GP modelling method is well-known as the Bayesian hierarchical Gaussian process (BHGP) [10, 42].

If source signals have non-smooth geometry, such as sharp changes, GP modelling of individual sets produces significant error compared to linear methods. Therefore, for non-smooth signals, $\hat{z}_2$ can be approximated using a linear model, *i.e.*

$$\hat{z}_2(x_i, y_i) = \boldsymbol{C\alpha}, \tag{40}$$

where $\boldsymbol{C}$ is the design matrix and $\boldsymbol{\alpha}$ are the modelling control parameters. Many mature interpolation and smoothing algorithms can be applicable for the approximation, including spline methods and Delaunay triangulation-based interpolation methods [36, 43-47].

In simplified cases, for example in which z_1 and z_2 have the same sample positions and the sample noise is small, $\hat{z}_2$ can simply be substituted by the source samples z_2. The linear approximation, given by equation (40) and the simple replacement by source samples, are highly efficient when the sample size is too large.

Based on the fusion models above, a fusion problem can be converted to an optimisation problem to find the optimal model parameters, which can be achieved by minimising the negative Gaussian likelihood [40, 48]. For example, in the BHGP method, the parameters $\{\beta_0, \beta_1, \beta_2, m_r, l_r, \sigma_r^2, \sigma_1^2\}$ are the objectives to deduce. The minimisation computation can be realised by using many well-known algorithms, such as interior-point methods [49] and trust-region-reflective methods, using MATLAB [50]. Another effective minimisation solution can be found in the GPML toolbox [51].

Based on the optimised parameters, fusion results can be calculated by introducing the two datasets as priors. The evaluation of the GP models above can be referred to the posterior estimation of GP functions [39], which is also a linear method, hence computationally efficient.

Figure 5-5 shows a comparison of a GP fusion result with the GP modelling results of individual sets without fusion. An optimised GP modelling of the LR set (blue '+') provides an LR estimation with a root-mean-square error (RMSE) of 0.133. An optimised GP modelling of the HR set (red '×') provides an HR estimation with an RMSE of 0.062. The GP fusion shows its success on the reduction of uncertainty, which offers a better estimation with less RMSE (down to 0.051).

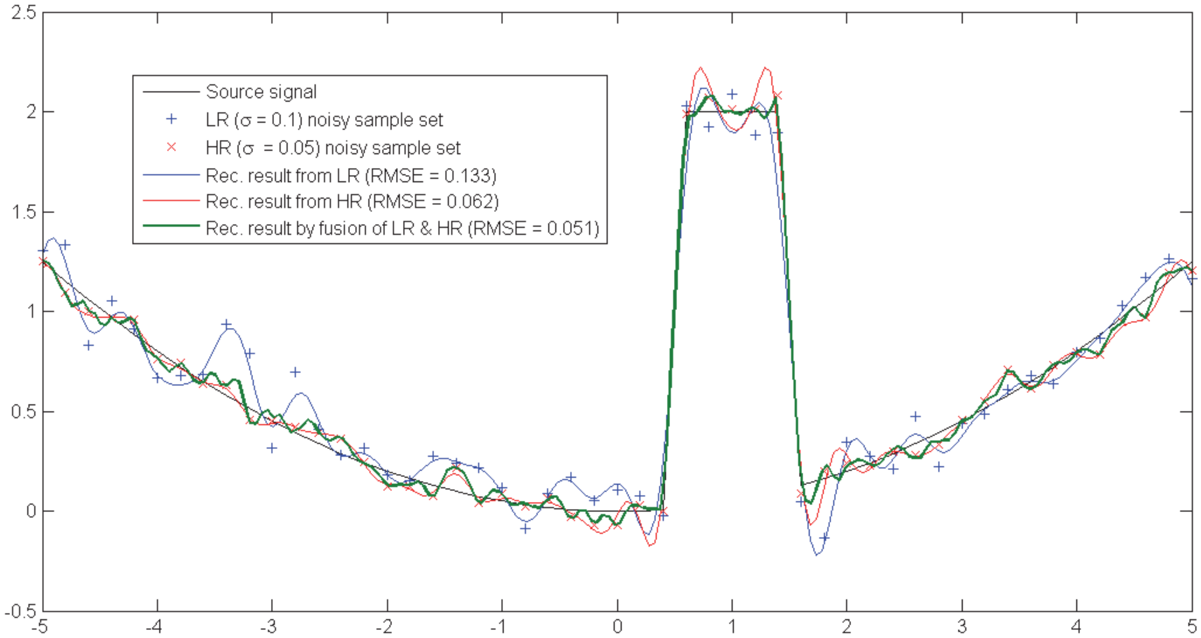

Figure 5-5. A GP fusion of two noisy datasets from a simple step signal with different noise levels.

Figure 5-6 shows another example of GP fusion for a freeform surface. A ten-by-ten HR dataset (red '×' in Figure 5-6a) and a twenty-by-twenty LR dataset (blue '+' in Figure 5-6a) are collected and fused based on an optimised BHGP model. As a reference, the HR and LR sets are individually modelled using optimised **0**-mean GP models, which present higher modelling accuracy for the freeform surface than general interpolation methods, such as Delaunay triangulation-based interpolation. For comparison, all the models are resampled on a twenty-by-twenty grid. The RMSE of the three models on the resampled positions demonstrates that GP fusion provides a significant reduction (about 25 %) of the measurement uncertainty from the individual modelling result with the lowest uncertainty.

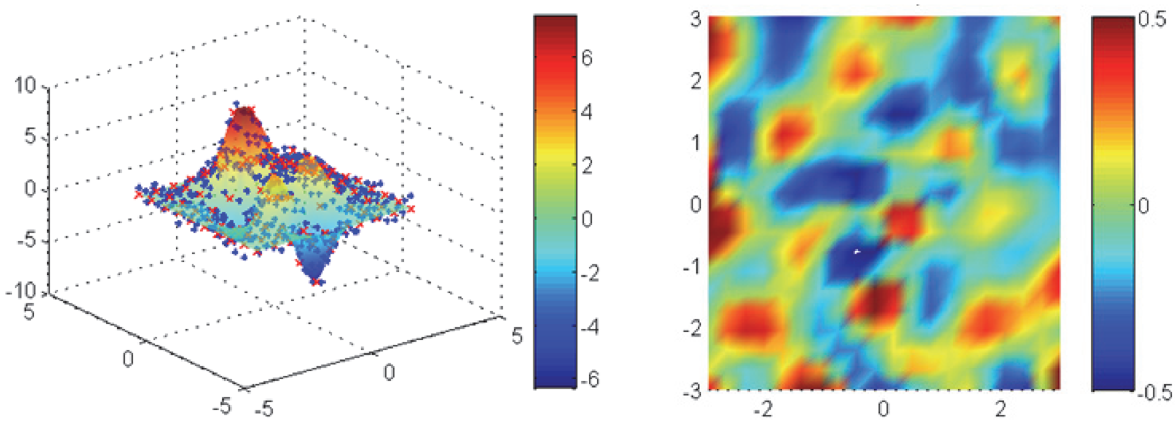

(a) The reference surface and the HR (red, σ = 0.1, 10 × 10) and LR (blue, σ = 0.2, 20 × 20) samples.

(b) The error map of an optimised GP model based on the LR set, RMSE = 0.237.

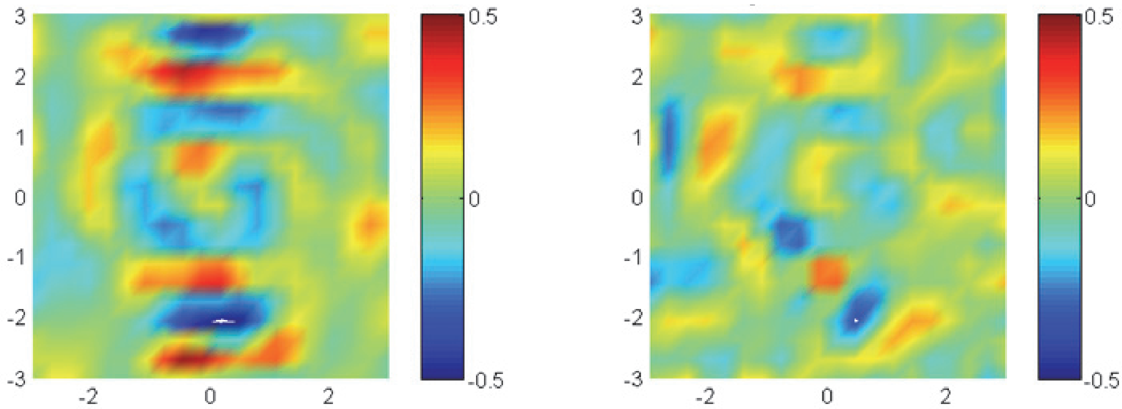

(c) The error map of an optimised GP model based on the HR set, RMSE = 0.141.

(d) The error map of an optimised BHGP fusion model, RMSE = 0.106.

Figure 5-6. A BHGP fusion of two noisy datasets from a freeform signal with different noise levels.

Figure 5-7 further shows a fusion example for a star pattern surface which is a typical example of a sharp-change signal. In Figure 5-7a, the yellow dots are 4665 samples drawn from a LR confocal microscope; the cyan crosses are 400 samples drawn from a HR 534 × 548 AFM data grid in random. Reconstructions of the individual sample sets are carried out based on Delaunay triangulations, the error maps of which, as obtained by resampling on the AFM 534 × 548 grid, are presented in Figure 5-7b and c. A GP fusion is obtained and its error map on the same resample positions is presented in Figure 5-7d, in which a reduced uncertainty can be found.

The simulations and experiments above demonstrate that GP fusion is a well-behaved fusion method. GP fusion, which uses one dataset as the mean and approximates the residuals of the two inputs using a GP, avoids miscellaneous designs of the parametric models for complex signals. Therefore, GP fusion is very useful for the measurement of complex signals, including non-smooth freeform or structured surfaces with sharp changes.

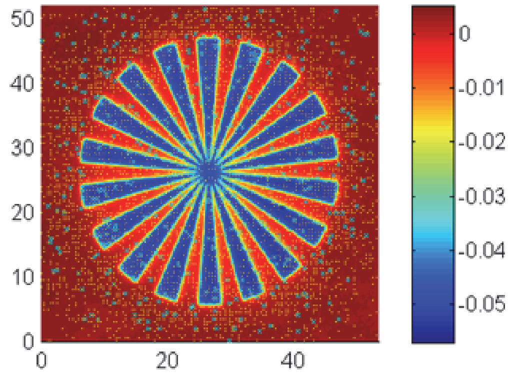

(a) The reference surface and the confocal (yellow, 4665 pts) and AFM (cyan, 400) samples.

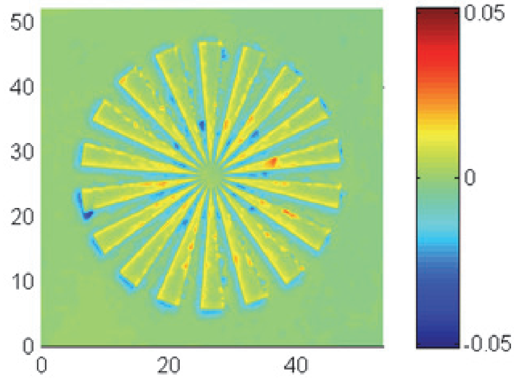

(b) The error map of a Delaunay reconstruction of the confocal set, RMSE = 6.2 nm.

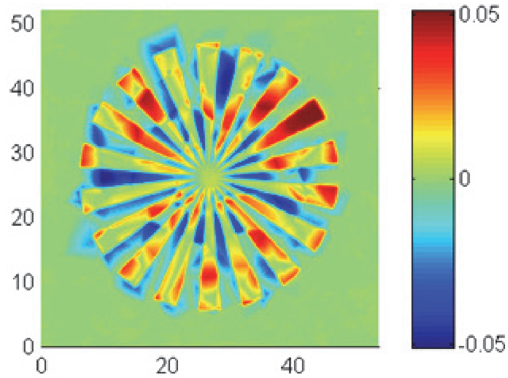

(c) The error map of a Delaunay reconstruction of the AFM set, RMSE = 13.6 nm.

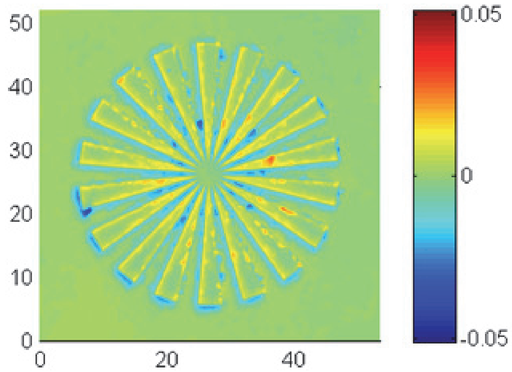

(d) The error map of a GP fusion model, RMSE = 5.9 nm.

Figure 5-7. A GP fusion of two noisy datasets with different noise levels from a structured surface.

5.3 A COMPARISON ON FUSION ACCURACY

Different fusion methods work in different ways which means they may have different performance characteristics for different applications. It has been stated elsewhere [8, 41] that GP fusion works effectively in the fusion of a higher reliability with lower sample density (HR&LD) set and a low reliability with higher sample density (LR&HD) set. The performance of GP fusion for other situations, for example in the fusion of a HR&HD set and a LR&LD set, or a HR&LD set and a LR&LD set, is unknown. Moreover, different fusion methods may work effectively for different signals. For example, GP fusion may be desirable for the fusion of sharp-change signals; WLS fusion may have higher fusion accuracy for smooth signals. The accuracy of WLS fusion and GP fusion are tested in this section.

Given an HR set and an LR set, with different sample densities (HD and LD respectively), fusion of the two sets has ten different combinations, for example, an LR&HD set versus an HR&LD set. Table 5-1 shows the ten combinations and a numbering of the situations is given for convenience in the report. In Table 5-1, the blue cells describe the four situations when the two input sets have the same density and same reliability level. The purple cells describe the two situations when the two input sets have different reliability levels but have the same density. The red cells describe the two situations when the input sets have different densities but have the same reliability level. The single green cell describes the fusion of an HR&LD set and an LR&HD set, while the central orange cell describes the fusion of an HR&HD set and an LR&LD set.

Table 5-1. Numbering of ten fusion situations.

Set 1 \ Set 2	LR&HD	HR&HD	LR&LD	HR&LD
LR&HD	1	2	3	4
HR&HD		5	6	7
LR&LD			8	9
HR&LD				10

To validate the performance of the 3DDF methods described in Section 5.2, two types of typical signals were simulated. The first is a randomly constructed smooth signal in a 3rd degree B-spline shift-invariant space [52], *i.e.*

$$f(x) = \sum_{k\in\mathbb{Z}^d} c_k\beta(x-k) : c\sim N(0,1), x \in [-5,5]. \quad (41)$$

where β_3 is 3rd degree B-spline basis function. The second is a step signal which is randomly positioned on a quadratic curve, such as in Figure 5-5, *i.e.*

$$f(x) = p_2(x) + f_{square}(x-t): t\sim U(-5,5), x \in [-5,5], \quad (42)$$

where $f_{square}(\cdot - t)$ is a standard square wave function centered at t and $p_2(x)$ is a 2nd degree polynomial function with fixed parameters.

Within each test, a source signal was initially constructed at random. Two sets of samples with different Gaussian noise were then collected at random positions. In other words, every simulation has varying conditions on the source signals, sample positions and sample noise. In the tests, LD and HD typically correspond to 25 and 51 in sample sizes; LR and HR correspond to 0.1 and 0.05 in the standard deviations of sample noise. After 100 simulations, the RMSEs of the fusion results were calculated with the best individual modelling results calculated as the reference.

Figure 5-8 shows the mean fusion errors and the standard deviations of the WLS fusion and BHGP fusion for the smooth signals in equation (41) under the ten fusion conditions in Table 5-1. Figure 5-9 shows the mean fusion errors and the standard deviations of the WLS fusion and BHGP fusion for non-smooth signals in equation (42) under the same ten fusion conditions.

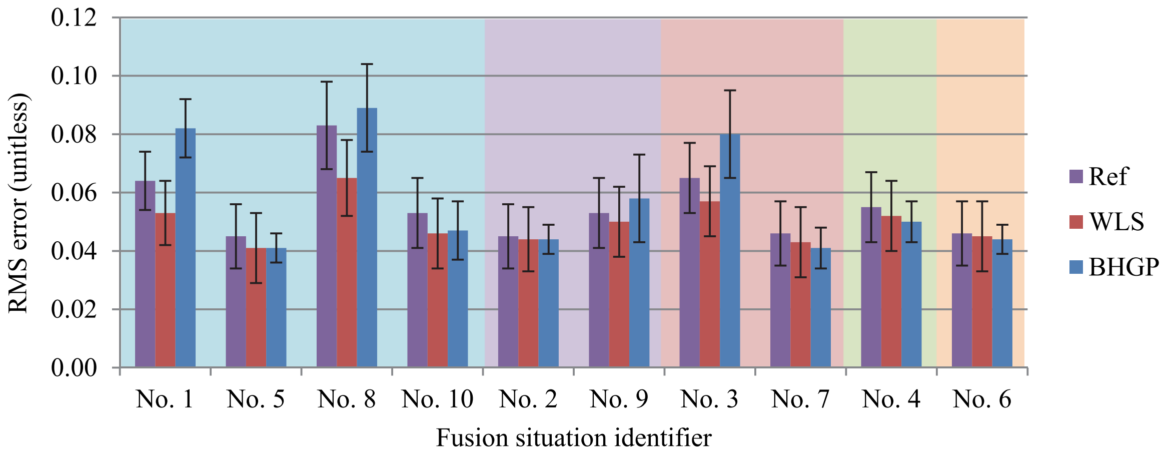

Figure 5-8. A comparison of the fusion errors of the WLS and GP fusion methods for B-spline smooth signals, for the situations in Table 5-1.

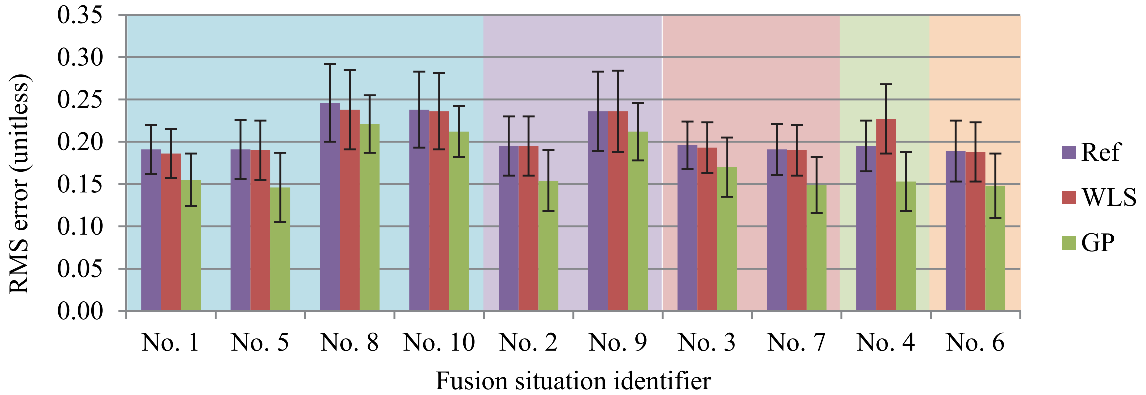

Figure 5-9. A comparison of the fusion errors of the WLS and GP fusion methods for step signals, for the situations in Table 5-1.

From the comparison, it can be observed that for non-smooth signals, GP fusion is usually the better method, which improves the fusion reliability with high probability. This observation is good evidence to support the application of GP fusion in the measurement of non-smooth signals, such as many structured surfaces.

For smooth signals, the WLS fusion is usually a better choice for most of the situations, except for the situations 4 and 6, in which the BHGP fusion performs slightly better. The fusion performance of a specific method in a specific situation usually involves high uncertainty. In particular, for the fusion situations 4 and 6 in Figure 5-8, the high uncertainty of the fusion performance of the WLS and BHGP fusion methods indicate that, in a considerable number of cases, the WLS method performs better than the BHGP method, though the BHGP has slightly lower mean fusion error in the 100 simulations. Therefore, the differences of the fusion performance of the tested methods for smooth signals are insignificant.

5.4 OTHER ISSUES

5.4.1 The data forms

3DDF tackles different forms of input data from a variety of instruments. Mixed forms of data, such as range images and point clouds, make a fusion algorithm complex to code and difficult to maintain. Conversion of different data forms into a common form is an important preparation step in a 3DDF framework.

Table 5-2 lists the general data forms used in current surface topography measuring instruments. The data forms are arranged and numbered according to their typical computation complexity (see the table title). Most of the data, for example the data from interferometry systems, AFM, focus variation systems, structured light scanners, stylus instruments and confocal microscopes, have the form of 2.5D range images as discussed in Section 4. Range images usually have high processing speed in numerical computations which are normally preferred. Other data formats include 3.5D volume data from CT, 3D point clouds, 3D grid data and 2.5D scattered data from CMMs, and 2.5D profile sets from stylus scanners. xD here means that a dataset has full degrees of freedom in x-dimensions. x.5D means that a dataset has $x + 1$ dimensions in total with one dimensional data being a function of the other two dimensional data. For example, 2.5D means that a dataset has three dimensions in total and one dimensional information is a dependent variable of the other two dimensional variables. Generally, a 3D surface can have arbitrary shape while a 2.5D surface cannot represent geometry with undercuts [32].

The convertibility between these data forms is illustrated in Figure 5-10. The green arrows denote that the conversion is a simple process; the red arrows indicate that the conversion needs complex manipulation. For example, the conversion from 2.5D scattered data to 3D point clouds is straightforward because 2.5D scattered dataset is a special 3D point cloud with no undercuts. In contrast, the conversion from 3D point clouds to 2.5D scattered data normally needs a rotation or projection process to avoid re-entrant features. For 3.5D volume data, its conversion to other 3D data needs complicated computational work, which can be referred to elsewhere [53, 54].

Because most of the data can easily be converted to 3D point clouds, and many advanced registration methods [55-57] tackle the data in 3D point cloud forms, 3D point clouds are the suggested common form in 3DDF. Recent work in [8] also expresses the same viewpoint.

Table 5-2. Generic data formats in surface measurement. ($M(\cdot)$ denotes the complexity of a matrix multiplication algorithm, m denotes the number of control parameters of the linear modelling).

No.	Name	Data storage	Instrument applications	Surface function models	Complexity in linear modelling
5	3.5D volume data	$[V]_{K\times L\times P\,(KLP=N)}$	XCT	Isosurface to be extracted out	Highly complex
4	3D point cloud	$\begin{bmatrix} X \\ Y \\ Z \end{bmatrix}_N$	CMM	$x_n = f_x(u_n, v_n)$, $y_n = f_y(u_n, v_n)$, $z_n = f_z(u_n, v_n)$.	$O(3M(m^2N))$
3	3D grid data	$\begin{Bmatrix} [X]_{K\times L} \\ [Y]_{K\times L} \\ [Z]_{K\times L} \end{Bmatrix}_{(KL=N)}$	CMM	$x_{k,l} = f_x(u_{k,l}, v_{k,l})$, $y_{k,l} = f_y(u_{k,l}, v_{k,l})$, $z_{k,l} = f_z(u_{k,l}, v_{k,l})$.	$\leq O(3M(m^2N))$
2	2.5D scattered data	$\begin{bmatrix} X \\ Y \\ Z \end{bmatrix}_N$	CMM	$z_n = f(x_n, y_n)$, $n = 1, \ldots, N$.	$O(M(m^2N))$
1	2.5D profile set	$\begin{Bmatrix} [Z]_{N_1} \\ [Z]_{N_2} \\ \vdots \\ [Z]_{N_K} \end{Bmatrix}_{(\sum N_k=N)}$	Stylus	$z_{k,n_k} = f(x_k, y_{n_k})$, $k = 1, \ldots, K$, $n_k = 1, \ldots, N_k$.	$\leq O(M(m^2N))$
0	2.5D range image	$[Z]_{K\times L\,(KL=N)}$	CSI, AFM, SL scanner, FV, confocal, stylus	$z_{k,l} = f(x_k, y_l)$, $k = 1, \ldots, K$, $l = 1, \ldots, L$.	$\leq O(M(m^2N))$

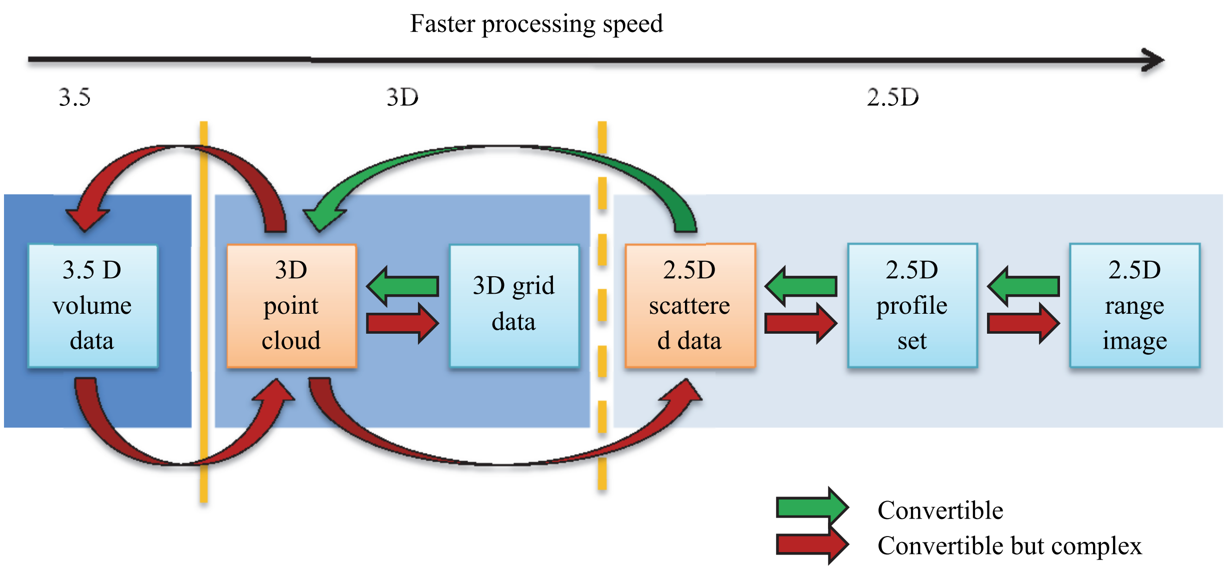

Figure 5-10. The convertibility between the general surface measurement data forms.

5.4.2 Post-fusion processes

In data fusion, there are normally three post-processes including data reduction, rendering and storage [11].

Once a fusion result is obtained, the original redundant datasets can be abandoned. Abandoning the original data saves storage space and avoids confusion when data rendering. In some situations, however, the original data needs to be retained for traceability. Therefore, data reduction is an optional process which is determined by the users' preferences.

Rendering of fusion datasets should provide fast and user-friendly vision interfaces. First, rendering of all the datasets in a specific field of view is not necessary due to the limitations of the computation speed. An indexing process to select the relevant datasets for a given field of view is needed. The indexed datasets for a field of view should only include the top surface datasets for a specific field of view. In 3DDF, the indexing needs more complicated solutions than range image fusion in which the indexing proceeds in a 2D plane. Meshing is another problem in rendering. A meshing process finds the neighbouring points for any point in a cloud, by which a point cloud can be rendered as a set of closely connected small facets. Meshing-based rendering can express the real-world entities in a vision-friendly way.

For storage, a fusion result can be expressed by a model with control parameters or digitised samples in Cartesian space. Expression by model parameters is obscure for understanding and needs decoding algorithms to convert them to spatial data. The existing variety of models, in particular non-parametric models, further increases the reading complexity of the fusion results. As an alternative, digitised sample points under specific sample conditions by using uniform sampling or intelligent sampling, provides an efficient and comprehensive solution for data storage.

All the post-processes need a specialised tool for management. An important capability of the data management tool is that it should be able to efficiently process a large amount of data. The examples in this report normally have two or several datasets to be considered. Practical situations are more complex. Currently, normal 3D measurements produce the measurement data in megabytes. It can be expected that an automated measurement of an engineered surface can produce the whole data in gigabytes or more, for example by stitching of hundreds to thousands of sub-aperture range images. Manipulation of large datasets may easily suffer the problem of slow processing and large memory storage requirements. An efficient database management system is needed for data fusion-based automated measurement, which is responsible for creation, updating, query and other administrations of the fusion data.

6 CONCLUSIONS AND FUTURE WORK

The existing data fusion solutions in surface topography measurement, which include repeated measurements fusion, stitching, range image fusion and 3DDF, were reviewed in this report with simulations. As an emerging application, 3DDF has received significant focus.

For 3DDF, GP fusion was found to have significantly better performance than WLS fusion for the measurement of non-smooth signals. GP fusion, which approximates a signal by using one input dataset as a prior guess, is usually better than WLS methods, which do not use an initial guess. For smooth signals, which can be well approximated using linear models, WLS fusion methods usually work better than GP fusion except in two situations, *i.e.* the fusion of HR&LD and LR&HD sets, and the fusion of HR&HD and LR&LD sets. This finding coincides with former research [8, 42].

Based on the reported work, future work on data fusion should concentrate on the following issues:

(1) Registration techniques for 3DDF were not well reviewed. Research on the selection of robust and flexible registration techniques for a mix of 3D point clouds and range images should be carried out.

(2) Monte Carlo simulation-based fusion methods, for example particle filters [1], which may be another promising solution for the fusion of non-smooth signals, should be carried out.

(3) The algorithms for rendering (dataset indexing and meshing) and storage of the fusion results based on a database management system need to be developed.

ACKNOWLEDGEMENT

This work was funded by the UK National Measurement System Engineering & Flow Metrology Programme, the FP7 project NANOMend, European Research Council (ERC-ADG-228117) and the UK's Engineering and Physical Sciences Research Council (EP/I033424/1).

REFERENCES

[1] Khaleghi B, Khamis A, Karray F O, Razavi S N 2013 Multisensor data fusion: a review of the state-of-the-art *Inform. Fusion* **14** 28-44

[2] Bruzzone A A G, Costa H L, Lonardo P M, Lucca D A 2008 Advances in engineered surfaces for functional performance *CIRP Ann.-Manuf. Techn.* **57** 750-69

[3] Evans C J, Bryan J B 1999 "Structured", "textured" or "engineered" surfaces *CIRP Ann.-Manuf. Techn.* **48** 541-56

[4] Jiang X, Scott P J, Whitehouse D J, Blunt L 2007 Paradigm shifts in surface metrology. Part II. The current shift Proc. R. Soc. A 463 2071-99.

[5] Leach R K, Jones C W, Sherlock B, Krysinski A 2013 The high dynamic range surface metrology challenge *28th ASPE Annual Meeting* 149-52

[6] Leica Microsystems 2014 Leica DCM8, URL: http://www.leica-microsystems.com/products/light-microscopes/industrial-materials/upright-microscopes/details/product/leica-dcm8/, accessed 01/09/2014

[7] Witec GmbH 2014 Automated confocal Raman and atomic force microscope alpha500, URL: http://www2.witec.de/products/raman/alpha500/, accessed 01/09/2014

[8] Colosimo B M, Pacella M, Senin N 2014 Multisensor data fusion via Gaussian process models for dimensional and geometric verification *Precis. Eng.* (In review)

[9] Ramasamy S K 2011 Multi-scale data fusion for surface metrology *PhD thesis* the University of North Carolina at Charlotte, USA

[10] Xia H, Ding Y, Mallick B K 2011 Bayesian hierarchical model for combining misaligned two-resolution metrology data *IIE Trans.* **43** 242-58

[11] Weckenmann A, Jiang X, Sommer K D, Neuschaefer-Rube U, Seewig J, Shaw L, et al. 2009 Multisensor data fusion in dimensional metrology *CIRP Ann.-Manuf. Techn.* **58** 701-21

[12] Boudjemaa R, Forbes A B 2004 Parameter estimation methods in data fusion *NPL Report* **CMSC 38/04**

[13] European Association of National Metrology Institutes 2010 EMRP call 2010 - industry & environment topic number SRT-02i: Multi-sensor data fusion in dimensional metrology *EURAMET*, URL: http://www.emrponline.eu/call2010/docs/srt/srt02i.pdf, accessed 01/09/2014

[14] Kelly G 2000 Data fusion special interest group, In: Ciarlini P, Forbes A B, Pavese F, Richter D *Advanced mathematical tools in metrology IV* 297-301 (World Scientific, Singapore).

[15] Esteban J, Starr A, Willetts R, Hannah P, Bryanston-Cross P 2005 A review of data fusion models and architectures: towards engineering guidelines *Neural Comput. Appl.* **14** 273-81

[16] Leach R 2014 *Fundamental Principles of Engineering Nanometrology (2nd ed.)* (Elsevier Science)

[17] Otsubo M, Okada K, Tsujiuchi J 1994 Measurement of large plane surface shapes by connecting small-aperture interferograms *Opt. Eng.* **33** 608-13.

[18] Zhao C, Burge J H 2008 Stitching of off-axis sub-aperture null measurements of an aspheric surface *Proc. SPIE* **7063** 16-1-7

[19] Zhang X 2009 Free-form surface fitting for precision coordinate metrology *PhD thesis* the University of Huddersfield, UK

[20] Kjer H M, Wilm J 2010 Evaluation of surface registration algorithms for PET motion correction *Master thesis* the Technical University of Denmark, Denmark

[21] Gruen A, Akca D 2005 Least squares 3D surface and curve matching *ISPRS J. Photogram.* **59** 151-74
[22] Weisstein E W 2014 "Mean": *MathWorld* – a Wolfram web resource
[23] Otsubo M, Okada K, Tsujiuchi J 1992 Measurement of large plane surface shape with interferometric aperture synthesis *Proc. SPIE* **1720** 444-7
[24] Catanzaro B E, Thomas J A, Cohen E J 2001 Comparison of full-aperture interferometry to subaperture stitched interferometry for a large-diameter fast mirror *Proc. SPIE* **4444** 224-37
[25] Chen S, Li S, Dai Y 2005 Iterative algorithm for subaperture stitching interferometry for general surfaces *J. Opt. Soc. Am. A* **22** 1929-36
[26] Chen S, Li S, Dai Y, Zheng Z 2007 Testing of large optical surfaces with subaperture stitching *Appl. Optics* **46** 3504-9
[27] Jiang X, Wang K, Gao F, Muhamedsalih H 2010 Fast surface measurement using wavelength scanning interferometry with compensation of environmental noise *Appl. Optics* **49** 2903-9
[28] Ramasamy S K, Raja J 2013 Performance evaluation of multi-scale data fusion methods for surface metrology domain *J. Manuf. Syst.* **32** 514-22
[29] Chen H, Liu Y Y, Wang Y J 2008 A novel image fusion method based on wavelet packet transform *2008 KAM Workshop*
[30] Chai Y M, Zhao R C, Ren J C 2004 Self-adaptive image fusion based on multi-resolution decomposition using wavelet packet analysis *ICMLC 2004*
[31] Yu S, Mantian L, Qingling L, Lining S 2006 A new wavelet based multi-focus image fusion scheme and its application on optical microscopy *ROBIO '06*
[32] Lonardo P M, Lucca D A, De Chiffre L 2002 Emerging trends in surface metrology *CIRP Ann.-Manuf. Techn.* **51** 701-23
[33] Huang Y, Qian X 2006 A dynamic sensing-and-modeling approach to three-dimensional point- and area-sensor integration *J. Manuf. Sci. Eng.* **129** 623-35
[34] Forbes A B 2012 Weighting observations from multi-sensor coordinate measuring systems *Meas. Sci. Technol.* **23** 025004
[35] Barker R M, Cox M G, Forbes A B, and Harris P M 2007 Software support for metrology best practice guide No. 4: Discrete modelling and experimental data analysis *NPL Report* **DEM-ES 018**
[36] de Boor C 2001 *A practical guide to splines* (Springer)
[37] Kalman R E 1960 A new approach to linear filtering and prediction problems *J. Basic Eng.* **82** 35-45
[38] Thacker N A, Lacey A J 2006 *Tutorial: The likelihood interpretation of the Kalman filter* (University of Manchester, UK)
[39] Welch G, Bishop G 1995 *An introduction to the Kalman filter* (University of North Carolina at Chapel Hill, USA)
[40] Rasmussen C E, Williams C 2006 *Gaussian processes for machine learning* (the MIT Press)
[41] Qian Z, Seepersad C C, Joseph V R, Allen J K, Jeff Wu C F 2005 Building surrogate models based on detailed and approximate simulations *J. Mech. Design* **128** 668-77
[42] Qian P Z G, Wu C F J 2008 Bayesian hierarchical modeling for integrating low-accuracy and high-accuracy experiments *Technometrics* **50** 192-204.
[43] Krystek M 1996 Form filtering by splines *Measurement* **18** 9-15
[44] Lee S, Wolberg G, Shin S Y 1997 Scattered data interpolation with multilevel B-splines *IEEE TVCG* **3** 228-44
[45] Hemsley R 2009 *Interpolation on a Magnetic Field*
[46] Raid I, Kusnezowa T, Seewig J 2013 Application of ordinary kriging for interpolation of micro-structured technical surfaces *Meas. Sci. Technol.* **24** 095201.
[47] Cazals F, Giesen J, Boissonnat J D, Teillaud M 2006 Delaunay triangulation based surface reconstruction, In: *Effective Computational Geometry for Curves and Surfaces* 231-76 (Springer Berlin Heidelberg).
[48] Santner T J, Williams B J, Notz W 2003 *The Design and Analysis of Computer Experiments* (Springer)
[49] Boyd S P, Vandenberghe L 2004 *Convex optimization* (Cambridge University Press)

[50] Mathworks 2014 *fmincon - Find minimum of constrained nonlinear multivariable function*

[51] Rasmussen C E, Nickisch H 2010 Gaussian processes for machine learning (GPML) toolbox *J. Mach. Learn. Res.* **11** 3011-5.

[52] Aldroubi A, Grochenig K 2001 Nonuniform sampling and reconstruction in shift-invariant spaces *SIAM Rev.* **43** 585-620

[53] Levoy M 1988 Display of surfaces from volume data *IEEE Comput. Graph.* **8** 29-37

[54] Hansen C D, Johnson C R 2005 *The visualization handbook* (Burlington, MA: Butterworth-Heinemann)

[55] Besl P J, McKay N D 1992 A method for registration of 3-D shapes *IEEE T. Pattern Anal.* **14** 239-56

[56] Zhang Z 1994 Iterative point matching for registration of free-form curves and surfaces *Int. J. Comput. Vision* **13** 119-52

[57] Low K L 2004 *Linear least-squares optimization for point-to-plane ICP surface registration* (University of North Carolina at Chapel Hill)